

Structural properties of subgroups of stars associated with open clusters

Jane Gregorio-Hetem^{1*}, Annibal Hetem²

¹Universidade de São Paulo, IAG, Rua do Matão 1226, 05508-090 São Paulo, SP, Brazil

²UFABC Federal University of ABC, Av. dos Estados, 5001, 09210-580 Santo André, SP, Brazil

Accepted 2024 July 27. Received 2024 July 27; in original form 2024 January 30.

ABSTRACT

Recent studies have identified star clusters with multiple components based on accurate spatial distributions and/or proper motions from *Gaia* DR3, utilising diverse diagnostics to improve our understanding of subgroup evolution. These findings motivated us to search for subgroups among the objects examined in our previous work, which employed fractal statistics. The present study considers seven open clusters that exhibit significant dispersion in age and/or proper motion distributions, suggesting that they would not be single clusters. For characterizing the stellar groups, we calculate the membership probability using Bayesian multi-dimensional analysis by fitting the observed proper motion distribution of the candidates. A probability distribution is also used to determine the distance of the cluster, which is obtained from the mean value of the distance modes. The photometry from *Gaia* DR3 is compared with evolutionary models to estimate the cluster age and total mass. In our sample, double components are found only for Markarian 38 and NGC 2659. The other five clusters are confirmed as being single. The structural parameters, such as Q , Λ_{MSR} and Σ_{LDR} are compared with results from N-body simulations to investigate how the morphology of the stellar clustering evolves. The new results, for a more complete sample of cluster members, provide a better definition of the distribution type (central concentration or substructured region) inferred from the $\overline{m} - \bar{s}$ plot.

Key words: stars: pre-main sequence – ISM: clouds – open clusters and associations: general.

1 INTRODUCTION

In the studies of stellar groupings, mass segregation and high surface density of sources are the properties typically expected in young star clusters. However, many stellar groups showing more or less concentrated clustering have been observed probably due to different conditions for star formation and dynamical evolution, such as NGC 2264 (González & Alfaro 2017), NGC 2548 (Vicente et al. 2016), NGC 6231 (Kuhn et al. 2017), NGC 3105 (Davidge 2017), and NGC 346 (Schmeja et al. 2009), among other examples. The formation of bound clusters or dispersed stellar groups depends on the initial physical condition of turbulence effects in a molecular cloud (Elmgreen 2008). For instance, recently formed clusters tend to follow the fractal structure of the clouds where they are found embedded (e.g. Elmgreen 2018).

Exploring the relationship between stellar groups and their natal star-forming regions hints at the hierarchical

structure of star distributions and cluster evolution. For instance, to systematically search for reliable small-scale structures in star-forming regions that could be related to the star formation process, González et al. (2021) developed a robust procedure to statistically analyse different regions having a varied sample of initial conditions. Their method was tested for synthetic and observed clusters, presenting successful results for regions with high degree of structures, where significant small-scale substructures were detected. For concentrated regions, they find a main structure surrounded by smaller ones. González et al. (2021) argue that multi-scale analysis is needed to disentangle the complexity of the region. In this work, we are particularly interested in clusters showing a low degree of structure, which could be evidence that structural characteristics may not change within the early stages of cluster evolution.

Hetem & Gregorio-Hetem (2019, hereafter HGH19) explored the fractal structure of a large sample of open clusters noticing some objects that seem to belong to larger groups due to the possible presence of separate components hav-

* E-mail: gregorio-hetem@usp.br (JGH)

ing slightly different values of parallax and proper motion. NGC 2659 is one of those considered in the literature as a single cluster (Dias et al. 2021; Cantat-Gaudin et al. 2018b; Poggio et al. 2021). However, in a study of the interaction of adjacent open clusters found in the Galaxy, which have spatial projected separation lower than 50 pc, Song et al. (2022) suggest NGC 2659 is a binary cluster.

Among the open clusters studied by HGH19, there are several objects for which it was suggested the possible presence of more than a single component. This hypothesis is due to the large deviations in the mean values of astrometric and dynamical parameters, as well as differences when comparing with results from the literature, meaning that subgroups appeared mixed and considered a single cluster. To explore the changes in structural parameters, we have selected a sample of clusters to be analysed in light of the possible presence of subgroups.

The paper is organized as follows. In Sections 2 and 3, we respectively present some of the literature results related to our sample and describe the data used to revisit previous studies. The analysis presented in Sect. 4 is based on characterizing stellar groups that depend on identifying the cluster membership, mode of distance, mass, and age. Section 5 is dedicated to the statistical analysis of the surface density distribution. In Sects. 6 and 7, we respectively present a comparison with previous results and summarize our conclusions. Finally, two appendices are included to present additional results (supplementary material available only in digital form).

2 SAMPLE SELECTION

For the revisiting analysis proposed here, we selected seven clusters from HGH19 with a larger number of members, which are listed in Table 1. We have searched the recent literature for the parameters to compare with our previous results (HGH19). Most of the parameters are presented by Cantat-Gaudin and collaborators, whose works are dedicated to studying the structure and history of the Milky Way by characterising open clusters and studying the Galactic disc using the distance, age, and interstellar reddening for stellar clusters identified with *Gaia* astrometry (e.g. Cantat-Gaudin et al. 2018a,b, 2020).

Our sample is also included in the list of clusters revisited by Dias et al. (2021), for which updated parameters are presented based on an isochrone fitting code (Monteiro et al. 2020) to the *Gaia* DR2 photometry, taking into account the nominal errors to derive distance, age, and extinction of each cluster. Bossini et al. (2019) also used the method of isochrone fitting to estimate visual extinction and age for part of our sample.

Poggio et al. (2021) used *Gaia* EDR3 data to map the segments of the nearest spiral arms in the Milky Way, based on the overdensity distribution of young upper main sequence stars, open clusters, and classic Cepheids. They used a list of open clusters from Cantat-Gaudin et al. (2020), but their analysis was restricted to the intrinsically bright objects, selecting the open clusters with more than five members with absolute magnitude $M_G \leq 0$. We notice that four of the objects in our sample (Collinder 205, NGC 2659,

NGC 2168, NGC 6494) coincide with the bright clusters present in the list of Poggio et al. (2021).

A machine learning code (SytaGO) was used by Pang et al. (2022) to study the hierarchical star formation process by analysing the three-dimensional morphology of young clusters, which revealed spatial and kinematic substructures. Two of our clusters appear in the sample studied by Pang et al. (2022): IC 2602 and NCG 3532; however, the morphology is indicated only for the second one, the “halo” type.

2.1 Previous results

In this section, we summarize individual comments for our sample to complement the information provided in Table 1. Similar information could not be included for all clusters due to varying availability in the literature searched.

- **Collinder 205:** The distance that was previously estimated by us for Collinder 205 (Col205 hereafter) is about 2 kpc (HGH19) in agreement with the value found by Cantat-Gaudin et al. (2018b), but is considerable larger than $d \sim 1.4$ kpc found by different works (Kharchenko et al. 2005; Dib et al. 2018; Dias et al. 2021) and smaller than $d \sim 2.4$ kpc presented by Poggio et al. (2021). There are also some discrepancies in our previous result of cluster age that tends to be younger than the ages found by other works (e.g. Cantat-Gaudin et al. 2020). Col205 was included in the Galactic mapping survey of chemical abundances of open clusters (Ray et al. 2022). As expected for clusters near the Sun, the metallicity ($[\text{Fe}/\text{H}] = -0.07 \pm 0.19$) and all other elements are within the normal of solar neighborhood cluster mean abundances. This result is consistent with $[\text{Fe}/\text{H}] = -0.169$ found by Dias et al. (2021).

- **IC 2602:** Density maps were obtained by Richer et al. (2021) with the method of fitting Gaussian functions to kernel density estimates, aiming to test in the solar vicinity the structural and dynamical early evolution theories, IC 2602 is one of the studied objects, which was considered a benchmark in this kind of test because it is one of the nearest clusters with ages ~ 50 Myr. Bravi et al. (2018) used the *Gaia*-ESO Survey (see Bragaglia et al. 2022, and references there in), products to estimate the gravity index, the lithium equivalent width, and the metallicity to identify candidate members for IC 2602. They also used the radial velocities to derive the cluster membership probabilities and the intrinsic velocity dispersion that changes from ~ 0.48 km s⁻¹ to ~ 0.20 km s⁻¹ depending on the number of members considered.

- **Markarian 38:** The estimates of proper motion and distance of the cluster Markarian 38 (hereafter Mrk38) presented by Poggio et al. (2021) are in excellent agreement with those from other works (Cantat-Gaudin & Anders 2020; Dias et al. 2021). An estimation of the morphological aspect is given by Hu et al. (2021b), indicating that the ellipticity ~ 0.13 is measured for both the core and the overall shape of the cluster. According to the study of morphological evolution of a sample of open clusters presented by Hu et al. (2021a), the overall shape of clusters becomes more elliptical as they grow older, while their core remains circular. This seems not to be the case for Mrk 38, whose core tends to be more elliptical.

- **NGC 2659:** Casado (2021) has explored the spatial distribution of *Gaia* sources aiming to identify possible double and multiple groups of star clusters, such as their “Group

Table 1. Coordinates, distance, astrometric parameters, age, and size found in the literature for the selected sample of open clusters.

cluster	α deg	δ deg	d pc	N	ϖ mas	μ_{α^*} mas yr ⁻¹	μ_{δ} mas yr ⁻¹	log(Age) yr	R deg	R ₅₀ deg	Reference
Col205	135.123	-48.983	2044	143	0.49	-4.81	3.94	5.7±2.1	0.10	...	HGH19
	135.091	-48.985	1400	99	0.46	-4.67	3.93	6.95	...	0.048	Dias et al. (2021)
	135.119	-48.984	1953	102	0.48	-4.80	3.92	0.047	Cantat-Gaudin et al. (2018b)
	135.119	-48.984	2394	80	0.54	-4.80	3.97	6.66	...	0.047	Poggio et al. (2021)
IC 2602	160.596	-64.419	154	140	6.49	-17.56	10.73	6.7±0.9	1.97	...	HGH19
	160.613	-64.426	152	311	6.60	-17.58	10.70	7.5	...	1.449	Cantat-Gaudin et al. (2018b); B19
	160.515	-64.444	151	318	...	-17.69	10.69	7.65	...	1.404	Pang et al. (2022)
	160.605	-64.399	...	30-99	6.70	8.0	Yen et al. (2018)
Mrk38	273.820	-19.004	1892	167	0.53	0.22	-1.75	6.55±0.9	0.05	...	HGH19
	273.812	-19.005	1770	26	0.56	0.85	-2.26	7.0	...	0.041	Dias et al. (2021)
	273.819	-18.997	1678	27	0.57	0.84	-2.28	7.0	...	0.044	Cantat-Gaudin & Anders (2020), P14
	273.819	-18.997	1802	17	0.56	0.81	-2.31	7.2	...	0.044	Poggio et al. (2021)
NGC 2168	92.267	24.310	887	127	1.13	2.22	-2.93	7.3±1.2	0.86	...	HGH19
	92.263	24.334	821	1215	1.13	2.30	-2.90	8.2	...	0.316	Dias et al. (2021)
	92.272	24.336	862	1325	1.13	2.31	-2.90	8.6	...	0.319	Cantat-Gaudin et al. (2018b), B19
	92.302	24.360	...	1239	1.12	0.62	-4.06	8.3	Cantat-Gaudin et al. (2018a)
NGC 2659	130.662	-44.975	2024	233	0.49	-3.99	3.59	6.5±1.41	0.12	...	HGH19
	130.633	-44.999	1815	91	0.43	-5.36	5.03	7.6	...	0.038	Dias et al. (2021)
	130.634	-44.999	2080	97	0.45	-5.34	5.03	7.4	...	0.042	Cantat-Gaudin et al. (2018b), B19
	130.634	-44.999	2095	82	0.47	-5.31	5.07	7.6	...	0.042	Poggio et al. (2021)
NGC 3532	166.489	-58.723	488	262	2.05	-10.41	4.99	6.6±0.9	0.54	...	HGH19
	166.412	-58.722	477	1762	2.06	-10.37	5.19	8.6	...	0.441	Dias et al. (2021)
	166.417	-58.707	477	1889	2.07	-10.38	5.17	0.536	Cantat-Gaudin et al. (2018b)
	166.389	-58.702	478	2559	2.10	-10.40	5.23	8.6	...	0.887	Pang et al. (2022)
NGC 6494	269.251	-18.969	740	170	1.35	0.55	-1.78	6.7±0.75	0.52	...	HGH19
	269.241	-18.969	691	694	1.36	0.28	-1.80	8.5	...	0.293	Dias et al. (2021)
	269.237	-18.987	674	789	1.35	0.28	-1.81	8.7	...	0.292	Cantat-Gaudin et al. (2018b), B19
	269.227	-19.000	...	53	1.23	1.17	0.09	8.5	Cantat-Gaudin et al. (2018a)

Notes: Results from Cantat-Gaudin et al. (2018b) are presented along with log(Age) adopted from Bossini et al. (2019, B19), when available. In the case of Mrk38, log(Age) is given by Piatti (2014, P14) complementing data from Cantat-Gaudin & Anders (2020). For IC2391, the results from Dias et al. (2021) are complemented by coordinates from Gaia Collaboration et al. (2018b). The size of the cluster is indicated by R₅₀ represents the radius of the area that contains 50 percent of members, excepting the results from Pang et al. (2022) that correspond to the half-mass radius.

18° that contains 8 open clusters. Four of these clusters were previously identified as a group by Liu & Pang (2019), including NGC 2659, which was suggested to constitute a pair with UBC 482. According to Song et al. (2022), this pair has similar values of proper motion and parallax but are 1° apart in the space distribution, corresponding to ~ 50 pc of projected separation. However, their distances exceed 250 pc (Poggio et al. 2021). For 82 members in NGC 2659 and 79 in UBC 482, Song et al. (2022) found ages of 44 Myr and 27 Myr, respectively.

• **NGC 3532:** The adopted age in the literature for NGC 3532 is ~ 300 Myr (Dobbie et al. 2009), but it was two orders of magnitude larger than the value estimated by HGH19. This cluster was included in the three-dimensional kinematic study by Jackson et al. (2022) to estimate the membership probabilities of open clusters. The morphology of NGC 3532 was studied by Hu et al. (2021a) giving the shape parameters corresponding to the ellipticity of the core $e_{core} = 0.074 \pm 0.031$ and of the cluster overall $e_{all} = 0.120 \pm 0.045$. Jadhav et al. (2021) identified the high mass ratio of binaries found in a sample of 23 open clusters to estimate their fraction and trace their radial segregation. Their results show that NGC 3532 is one of the clusters with the lowest frac-

tion of high mass-ratio binaries compared to the rest of the population. These results agree with Li et al. (2020), arguing that NGC 3532 is not a binary-rich cluster, and its binary mass ratio follows a nearly uniform distribution.

• **NGC 6494:** Cordoni et al. (2023) infer a core radius $r_c = 1.8$ pc and $A_V = 1.28$ mag considering 1273 members in NGC 6494. Tarricq et al. (2022) analysed a sample of 870 members and obtained $r_c = 2.55$ pc, where the core has low eccentricity, while the halo has an elongated distribution, such as a tail-like structure with semi-major axis = 16.5 pc and a semi-minor axis = 6.29 pc. A comparable result was found by Hu et al. (2021b), estimating for NGC 6494 a value of 0.15 for the ellipticity of the core. Rain et al. (2021) and Bossini et al. (2019) have adopted extinction correction, respectively $E(B-V) = 0.27$ and $A_V = 0.85$ mag that coincide with the values used by us. The age estimated by HGH19 is lower than the range of 380 Myr to 479 Myr (e.g. Spina et al. 2021; Poggio et al. 2021; Rain et al. 2021).

The examples above are the primary sources used for parameter comparison (see Table 1). Our criteria for sample selection were based on the large differences found among our previous results and the literature, suggesting that discrepancies in the parameters and/or large uncertainties

could indicate more than one structure in these selected clusters, possibly not noticed by HGH19. The data used in our analysis are described as follows.

3 DATA SETS

3.1 Optical data

The astrometric and photometric data was obtained from *Gaia* DR3 (Gaia Collaboration et al. 2023) by adopting query ranges defined on the basis of parameters estimated by HGH19: J2000 equatorial coordinates (α , δ), parallax (ϖ), and proper motion (μ_{α^*} , μ_{δ}), where $\mu_{\alpha^*} \equiv \mu_{\alpha} \cos \delta$. Table 1 gives the adopted position and size of the clusters, compared with other results from the literature.

Using the positions given in Table 1, we searched for all the sources in the area defined by a radius 10 percent larger than the cluster radius (HGH19). To avoid *Gaia* sources showing low quality of the astrometric solution, the selection was restricted to objects having $\text{RUWE}^1 < 1.4$.

To estimate individual mass and age of the cluster members, we constructed Colour-Magnitude Diagrams (see Sect. 4.3) with photometric data at bands G (~ 639 nm), G_{BP} (~ 518 nm), and G_{RP} (~ 782 nm) from *Gaia* DR3. The observed apparent magnitudes were corrected for extinction based on reddening $E(G_{BP} - G_{RP})$ that is derived from A_0 , the line-of-sight extinction available for some of the *Gaia* sources. A_0 is one of the stellar parameters inferred by the algorithm Aeneas that is part of the package GSP-Phot (General Stellar Parametrizer from Photometry)². The method performed by Aeneas consists of a simultaneous fitting of the observed parallax, BP/RP spectra, and apparent magnitude (*Gaia* G band) using the technique of Bayesian posterior maximisation.

In the case of sources with no reddening information given by the *Gaia* catalogue, we estimate the colour excess $E(B - V)$ based on the colour-magnitude diagram by fitting the observed unreddened magnitudes to the distribution of magnitudes that were corrected by the algorithm Aeneas. The value of $E(B - V)$ that gives the best fitting was used to infer a mean value for visual extinction (A_V) by adopting $R = \frac{A_V}{E(B - V)} = 3.1$ (Savage & Mathis 1979). We checked the validity of the mean values of A_V by inspecting the extinction maps provided by Dobashi et al. (2005), discussed in Sect. 3.3. The conversion between A_V and the expected extinction at the *Gaia* photometric bands was adopted from Casagrande & VandenBerg (2018).

3.2 Infrared photometry and mapping

We checked in our sample the occurrence of circumstellar dust emission to identify the cluster members that are disc-bearing stars. Large infrared excess is expected for Young Stellar Objects (YSOs) that still are embedded in their natal cloud (Class 0 objects), as well as for pre-Main Sequence stars with large amounts of circumstellar dust (Class I and

Class II). Considering that protostellar discs only survive up to a few tens of Myr, members of older clusters are expected to be Class III objects (without discs). The classification based on the emission at near- and mid-infrared confirms the evolutive status of the clusters and could help identify the presence of mixed populations (different ages) in the sample. In Appendix A (supplementary material), we describe the search for disc-bearing sources performed by fetching from public catalogues the infrared counterparts of the *Gaia* sources. A cross-matching between the position of the sources was performed on the 2MASS (The Two Micron All Sky Survey, Cutri et al. 2003; Skrutskie et al. 2006), and All-WISE (Wide-field Infrared Survey Explorer, Wright et al. 2010; Cutri et al. 2013) catalogues. The observed magnitudes at 2MASS (JHK) and WISE (W1: 3.35 μm ; W2: 4.6 μm , W3: 11.6 μm) bands were fetched only for the sources showing flags indicating good photometric quality and data that are unaffected by known artifacts.

Aiming to inspect the dust distribution in the direction of the clusters, we searched for the continuum images at 70-500 μm obtained by the *Herschel* Infrared Galactic Plane Survey (Hi-GAL, Molinari et al. 2010). We found only two $\sim 2^\circ$ strip tiles covering objects of our sample: Fields 264 and 269, respectively, containing the clusters NGC 2659 and Collinder 205. A third cluster, Mrk38, is found near the southeast corner of Hi-GAL Field 11 but outside the image (see Fig. B1, supplementary material). In this case, it is not possible to directly infer the local infrared emission. However, we could verify the lack of dust emission at this corner of Field 11 and around its neighborhood (Hi-GAL Field 13). Inspecting the far-infrared maps gives us some clues that the dust distribution is in good agreement with the visual extinction maps, as discussed in the following.

3.3 Visual extinction maps

The dust distribution in the Galaxy is related to the A_V maps and traces the gas distribution in molecular clouds.

Among the existing dust-based maps, there are two of our particular interest: the visual extinction maps from Dobashi et al. (2005), and the column density mapping derived from the Hi-GAL survey (Marsh et al. 2017) using the point process mapping (PPMAP)³ described by Marsh et al. (2015). In this case, the *Herschel* images of dust continuum emission are used to produce image cubes of differential column density as a function of dust temperature and position.

In this work we use the A_V maps⁴ produced from the optical DSS⁵ images (Dobashi et al. 2005), in spite of their lower resolution ($\sim 6'$ pixel⁻¹) than the extinction maps based on 2MASS data ($\sim 1'$ pixel⁻¹, Dobashi 2011). This choice was made to avoid unreal ($A_V < 0$) values that could occur in some regions mapped by using near-infrared photometry, which is not the case in the DSS maps.

Since we are interested in a rough estimation of A_V , to be used to check the reddening correction (see Sect. 4.3), we can consider the comparison between dust extinction maps produced from different data sets as a confirmation that the

¹ Re-normalised unit weight error (see details in the technical note GAIA-C3-TN-LU-LL-124-01).

² Details are found in the *Gaia* DR3 documentation (Sect. 11.3.3) at <https://gea.esac.esa.int/archive/documentation/GDR3/>.

³ <https://www.astro.cf.ac.uk/research/ViaLactea/>.

⁴ <https://darkclouds.u-gakugei.ac.jp>.

⁵ Digitized Sky Survey - STScI/NASA.

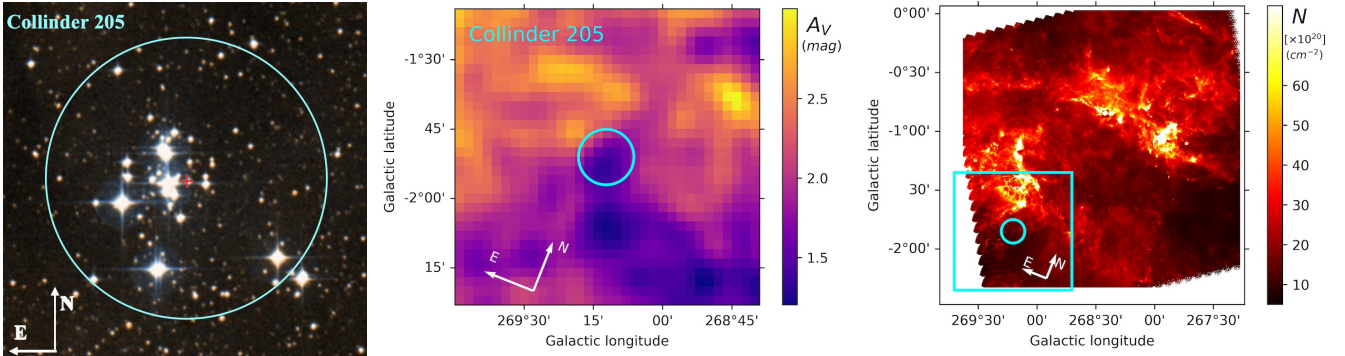


Figure 1. The field-of-view of Col205 (cluster radius = $6'$, cyan circle). *Left:* Optical image (DSS coloured, SIMBAD database) centered at equatorial coordinates given in Table 1. *Middle:* Visual extinction map presented in galactic coordinates, obtained by Dobashi et al. (2005) based on DSS images. The arrows show the equatorial coordinates direction, and the circle is the same as the left panel. *Right:* Integrated column density map of hydrogen molecules estimated from HI-GAL based maps of dust continuum emission (Herschel PPMAP). The cyan square approximately corresponds to the same area seen in the middle panel.

position of the clusters coincides (or not) with regions showing low levels of dust concentrations.

Aiming to illustrate the use of the A_V maps as a diagnosis of the presence of dust concentration, in Fig. 1 we compare the maps from Dobashi et al. (2005) with the *Herschel* PPMAP, presented in the form of 2D map of integrated line-of-sight column density of hydrogen molecules (in units of 10^{20} cm^{-2}). In Table 2, we present the range of extinction values inferred by visual inspection of the A_V maps. The values of $E(B-V)$ used to correct the reddening (as discussed in Sect. 3.1) are also presented in Table 2, which are in good agreement with the estimates from the A_V maps, excepting NGC 2659, which shows $E(B-V)$ that is 0.19 mag larger than the value expected from the extinction map.

4 CHARACTERIZATION OF STELLAR GROUPS

The optical data extracted from the *Gaia* DR3 catalog (see Sect. 3.1) were used for three purposes: to analyze the vector-point diagram (VPD) constructed using proper motion (μ_{α^*} , μ_{δ}) of the stars to identify the members of different groups; using the parallax (ϖ) measured for the members to estimate the distance mode; and determining cluster age and individual stellar masses from isochrones fitting in the optical colour-magnitude diagram. The following sections are dedicated to describing the adopted methodology for identifying structures, the characterization of the clusters, and their respective stellar content.

4.1 Membership probability

In the literature, the search for substructures has been conducted using methods and techniques based on spatial and kinematic analyses to identify discrete structures (e.g., Kuhn et al. 2014; González et al. 2021; Buckner et al. 2022b, 2024), spatial stellar associations (e.g., Buckner et al. 2019), or dynamical analyses (e.g., Kuhn et al. 2019; Buckner et al. 2020, 2024), among other approaches. Young star clusters that are no longer embedded in their natal molecular cloud (10-50 Myr, e.g. Bica et al. 2019) are not expected to exhibit

overdensities in their spatial distribution, which requires different criteria to identify which stars are physically related members confidently. Common velocities and distance are the main characteristics that stars inherit from the original cloud, giving the cluster a coeval movement until the tidal disruption that destroys the cluster (Lada & Lada 2003).

In this work, we adopt the method from Sanders (1971) for identifying cluster members by their proper motion modeled according to a Probability Distribution Function (PDF), following the formalism presented by Dias et al. (2014). It was adopted as a segregation procedure based on a mixed bivariate density function model for proper motions, considering that the cluster and the field are independent, as suggested by Uribe & Brieva (1994).

We adopted a PDF model that considers a sum of normal distributions, whose number of components can be two (cluster+field) or three (2 subclusters+field). The choice depends on visual inspection of proper motion VPD. Considering that candidates are projected against the same area, they do not present large differences in spatial distributions that could help distinguish subclusters. By this way, the only other parameter considered is parallax. The resulting PDFs are defined by the mean, standard deviation, and correlations for proper motion and parallax.

In summary, the membership probability is defined by using the maximum likelihood method that depends on the contrast between cluster members and field-stars. Accurate membership probabilities can be achieved by using Bayesian multi-dimensional analysis and performing a global optimization procedure based on the Cross-Entropy technique (Rubinstein 1997), to fit the observed distribution of proper motions and to obtain the probability of a given star belonging or not to the cluster. We also used a genetic algorithm to improve the first guess of the parameters set. HGH19 gives details on the membership probability calculation.

Our analysis is restricted to the samples of stars with 50 percent or more of membership probability, which will be hereafter referred to as P_{50} members or simply members. The mean values for the parameters estimated for the clusters are presented in Table 2. Among the objects we studied, only for Mrk38 and NGC 2659 we found a second group in the same studied region. In these cases of double groups, the

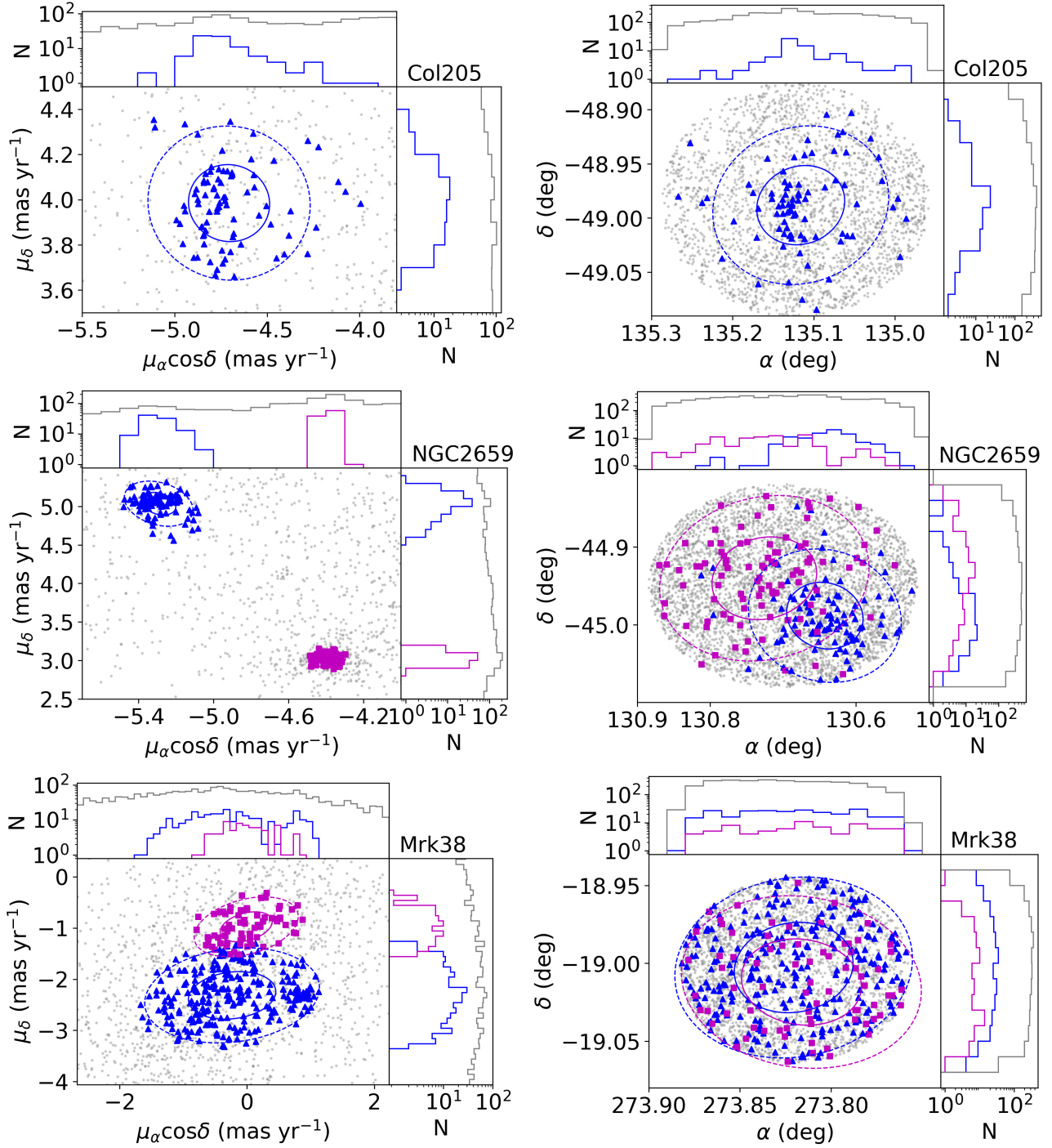


Figure 2. Vector point diagram of proper motion (*left panel*) and the spatial distribution (*right panel*) for all the selected *Gaia* sources (grey dots) and the P_{50} members (blue triangles). Magenta symbols are used for NGC 2659b and Mrk38b. The ellipses indicate the standard deviation of the mean values (1σ : full lines, 2σ : dashed lines). The histograms show the distribution of number of members and field stars.

main cluster is denoted by index a and the secondary group by b .

The distribution of members in the proper motion VPD and their position in the plot of equatorial coordinates are shown in Fig. 2 for Collinder 205 (hereafter Col205), a repre-

sentative of single clusters⁶, and the two targets that were found bimodal. The main criteria for choosing the single or two-component clusters are based on the separation of groups showing different proper motions. This separation is

⁶ The figures corresponding to the other clusters of the sample are given in Appendix B (supplementary material)

also evidenced by the mean values of proper motion and distances shown for each subgroup in Table 2. Despite the clear separation on proper motion, the spatial distribution of the members of the two groups associated with NGC 2659 roughly covers the same projected area, with a slight trend of subgroup *a* being more concentrated in the SW region, while subgroup *b* tends to the NE region. On the other hand, both components of Mrk38 occupy the same projected area without any separation in the plot of equatorial coordinates.

Another criterion confirming the cluster membership is based on the mean value of the parallax (ϖ). In Fig. 3 (top panel), we present the distribution of ϖ as a function of apparent magnitude in band G, using different colour grades to indicate membership of Col205. It can be noted that the most probable members show a narrow distribution around $\varpi \sim 0.5$ mas, mainly for the brighter sources ($G < 17$ mag). Fainter objects, for which the membership probability is lower, show a dispersion around the mean value of ϖ . To infer the distances of the clusters, we adopted a statistical methodology based on a parallax distribution, which is described below.

4.2 The most probable distance

We discuss here the procedure to improve the distance determination based on *Gaia* parallax of objects at kilo-parsec scale distances. In this case, the simple method of inversion of ϖ does not give accurate results, mainly for objects having high fractional parallax uncertainty, defined as $f = \sigma_{\varpi}/\varpi$. According to Luri et al. (2018), the estimation by the inversion of the parallax tends to overestimate the distance modulus, which is a poor approximation due to systematics and correlations in the *Gaia* astrometric solution.

For instance, the use of model fitting to obtain the PDF by an automated Bayesian approach (BASE-9) was adopted by Bossini et al. (2019) to infer the distance modulus and estimate the age for 268 open clusters. They found a median offset of -0.11 mag for the difference between the distance moduli derived from the analysis of BASE-9 results and the inversion of the median parallax.

Navarete et al. (2019) also used a Bayesian inference method to estimate the distance to the W3 complex ($d = 2.14$ kpc). They derived the PDF by adopting the exponentially decreasing space density suggested by Bailer-Jones (2015). The distances found for W3 and its substructures, considering the median value of the PDF, are about 5 percent different from those obtained by the simple inversion of parallaxes. For a more extreme case, the massive stellar cluster Westerlund 1 (Wd 1), Navarete et al. (2022) revisited the distance estimation by using *Gaia* EDR3 and considering new cluster members. They inferred an improved distance of 4.06 kpc for Wd 1, adopting the parallax method suggested by Cantat-Gaudin et al. (2018b) when dealing with cluster members with large uncertainties on the individual parallaxes. In these cases, the distance is assumed to be the same for all the cluster members and is calculated by following a maximum-likelihood procedure (see Eq. 1 from Cantat-Gaudin et al. 2018b).

In Fig. 3 (bottom panel), we show the plot of f as a function of G magnitude, aiming to evaluate, among the objects of our sample, the occurrence of observed parallaxes with large fractional parallax uncertainty. We verified that

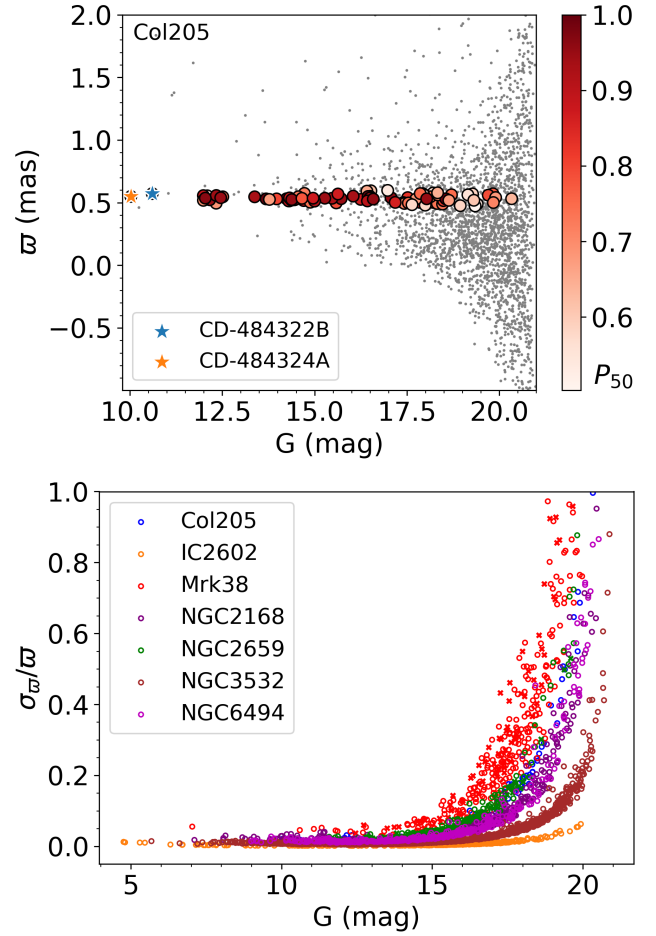


Figure 3. *Top:* Plot of parallax as a function of G magnitude and the membership probability (colour-bar scale), highlighting two of the brightest stars of Col205. *Bottom:* The fractional parallax uncertainty ($f = \sigma_{\varpi}/\varpi$) as a function of G magnitude. Members of the secondary group of double clusters are indicated by \times . Faint objects ($G \sim 18$ mag, depending on distance) have $f > 0.3$, which occurs for a minor part of the members, except Mrk38.

only the faint ($G > 18$ mag) members of our clusters may present high parallax uncertainty ($f > 0.3$), which occurs for less than 20 percent of the members, excepting for Mrk38a and Mrk38b that have more than 50 percent of their members showing $f > 0.3$.

Considering that most objects in our sample do not show extreme cases of high fractional parallax uncertainty, we calculate the distance for each cluster member by using a simple PDF to estimate the true distance $d = 1/\varpi_{\text{true}}$ based on the observed parallax (ϖ). For the individual distance estimation, we adopt the probability distribution suggested by Luri et al. (2018), assuming that the observed parallax is normally distributed around the true parallax:

$$p(\rho|\varpi_{\text{true}}) = \frac{1}{(2\pi \rho^4 \sigma_{\varpi}^2)^{0.5}} \exp\left(-\frac{(1/\rho - \varpi_{\text{true}})^2}{2\sigma_{\varpi}^2}\right), \quad (1)$$

where $\rho = 1/\varpi$ and σ_{ϖ} is the uncertainty on the individual observed parallax. The mode of the distribution was obtained for each member of the cluster, and finally, we calculated the mean value of the modes that is adopted as the

distance of the whole cluster. Figure 4 displays histograms of the distribution of distance modes, whose mean values are presented in Table 2. Only the members with low fractional parallax uncertainty ($f < 0.3$) were considered in the calculation of the mean value of distance modes.

4.3 Colour-Magnitude diagrams

We used the photometric data from *Gaia* DR3 to compare the observed colours and magnitudes of the cluster members with theoretical isochrones that give us an estimation of stellar mass and age. The isochrones were adopted from *PARSEC*⁷ evolutive models (Bressan et al. 2012; Marigo et al. 2017), which were plotted in the $(M_G)_0 \times [G_{BP} - G_{RP}]_0$ diagram, where the absolute magnitude was estimated by adopting for all the stars the same value of distance inferred for the cluster (see Sect. 4.2). The observed apparent magnitudes were corrected for extinction following the procedure described in Sect. 3.1. Figure 5 shows the distribution of *Gaia* sources in the colour-magnitude diagram, compared with the *PARSEC* isochrone that provides a good fitting of the observed data, which was adopted as the cluster age. The uncertainty on the age is indicated by the grey area shown in Fig. 5, which is defined by lower and upper isochrones encompassing the distribution of data points.

Stellar mass for each cluster member was estimated by adopting a simple interpolation method based on algebraic fitting inside the regions delimited by the intersection between the theoretical lines (isochrones and evolutionary tracks). By localizing the observed position of a given star on the colour-magnitude diagram, the method infers the value of the mass by interpolating the theoretical values from the two nearest evolutionary tracks. The sum of the individual masses obtains the total observed mass of the cluster.

To validate the results derived from the colour-magnitude diagrams, in Fig. 6, we plot the individual masses (estimated by us) as a function of effective temperature (provided by *Gaia*) for Col205. Fig. B5 (supplementary material) shows the plots for the other single clusters of our sample. As an illustration, the theoretical lines corresponding to three examples of isochrones from stellar models are also plotted. It can be noted a good mass-temperature correlation of low-mass stars ($< 2 M_\odot$) following a main sequence, while some massive stars having low temperature coincide with the Red Giants region, as shown by the isochrones of 119 Myr (two members of NGC 2168), and 300 Myr (NGC 6494).

The good agreement among the parameters, obtained from different databases (*Gaia*, *PARSEC*) and the individual masses estimated by us, gives confidence on the observed mass of the cluster.

A similar confirmation is obtained when comparing the isochrone corresponding to the cluster age with the distribution of observed G magnitude as a function of the effective temperature (T_{eff}) shown in Fig. 7. It is interesting to note the expected dispersion due to the presence of binary stars. In the case of NGC 3532, the separation of binaries is very clear and can be fitted by the same isochrone, but using an

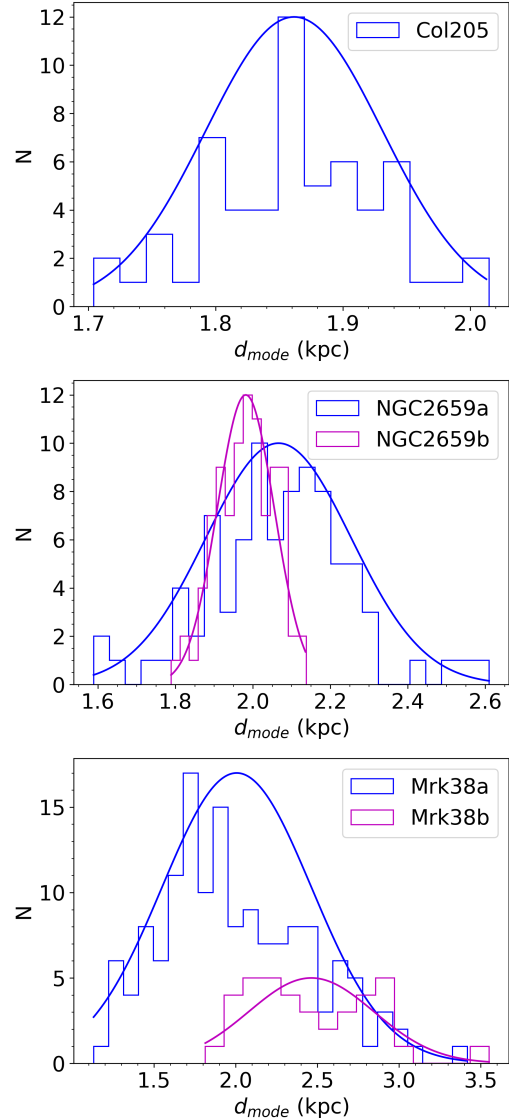


Figure 4. Distance mode histogram obtained for Col205, NGC 2659 and Mrk38, excluding P_{50} members that have fractional parallax uncertainty $f < 0.3$. The curves show the Gaussian fitting used to determine the mean value adopted as the cluster distance.

offset of $\Delta G = 0.75$ mag. According to the simulations performed by Donada et al. (2023) using evolutive models that include unresolved binaries in the Main Sequence population, this offset best fits the secondary distribution in the $G \times [BP - RP]$ diagram.

4.4 Mass function

The results for the sample containing only P_{50} members give accurate mean values of astrometric parameters, distance, and age of the cluster. However, the incompleteness of the sample has an impact on the correct estimation of parameters depending on total mass, such as crossing time and dynamical age, as well as for the cluster size and core radius derived from the fitting of the surface density distribution (see Sect. 5.1).

⁷ Version v1.2S+COLIBRI PR16 of *PARSEC* models available on <http://stev.oapd.inaf.it/cgi-bin/cmd>.

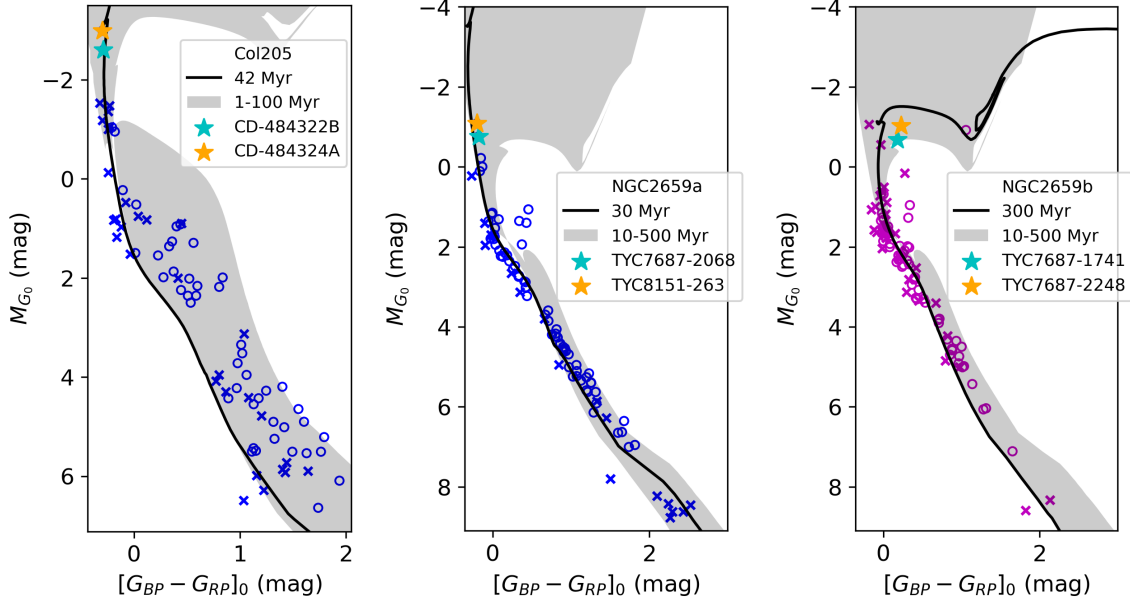


Figure 5. Colour-Magnitude Diagram for P_{50} members compared with isochrones from PARSEC models that best fit the cluster age. The *Gaia* photometric data are unreddened by using the extinction correction estimated by the algorithm Aeneas (open circles). For the sources without Aeneas correction (\times symbols), we adopted a mean value for $E(B-V)$ (see Sect. 3.1).

Table 2. Parameters estimated for the P_{50} members of the clusters, and A_V ranges obtained from the visual extinction maps.

Cluster	α (2000) deg	δ (2000) deg	$\mu_{\alpha} \cos \delta$ mas yr $^{-1}$	μ_{δ} mas yr $^{-1}$	d pc	N_{P50}	R_{P50} pc	M_{P50} M_{\odot}	age Myr	$E(B-V)$ mag	A_V map mag
Col205	135.116 \pm 0.054	-48.988 \pm 0.036	-4.71 \pm 0.22	3.98 \pm 0.17	1862 \pm 70	83	3.26 \pm 0.15	170	42	0.89	1.5 - 2.5
IC2602	160.899 \pm 2.101	-64.523 \pm 0.778	-17.75 \pm 0.94	10.64 \pm 0.97	152 \pm 3	295	8.17 \pm 0.14	197	119	0.10	0 - 1.0
Mrk38a	273.821 \pm 0.032	-19.003 \pm 0.029	-0.23 \pm 0.69	-2.32 \pm 0.46	1984 \pm 455	271	1.77 \pm 0.01	265	20	0.34	0 - 1.0
Mrk38b	273.816 \pm 0.033	-19.012 \pm 0.028	-0.01 \pm 0.41	-0.98 \pm 0.29	2461 \pm 382	75	2.01 \pm 0.05	76	250	0.34	0 - 1.0
NGC2168	92.273 \pm 0.3	24.342 \pm 0.289	2.22 \pm 0.17	-2.9 \pm 0.15	861 \pm 29	845	13.7 \pm 0.2	1056	119	0.28	0 - 0.5
NGC2659a	130.643 \pm 0.052	-44.988 \pm 0.043	-5.29 \pm 0.09	5.04 \pm 0.15	2066 \pm 189	98	4.06 \pm 0.18	140	30	0.51	0.75 - 1.0
NGC2659b	130.726 \pm 0.071	-44.94 \pm 0.053	-4.39 \pm 0.05	3.03 \pm 0.06	1979 \pm 78	96	4.64 \pm 0.14	174	300	0.51	0.75 - 1.0
NGC3532	166.46 \pm 0.484	-58.705 \pm 0.243	-10.42 \pm 0.4	5.22 \pm 0.38	477 \pm 11	1262	6.68 \pm 0.03	1218	300	0.07	0.5 - 1.0
NGC6494	269.252 \pm 0.244	-18.989 \pm 0.233	0.35 \pm 0.15	-1.84 \pm 0.16	741 \pm 21	424	7.02 \pm 0.06	530	250	0.45	1.5 - 2.0

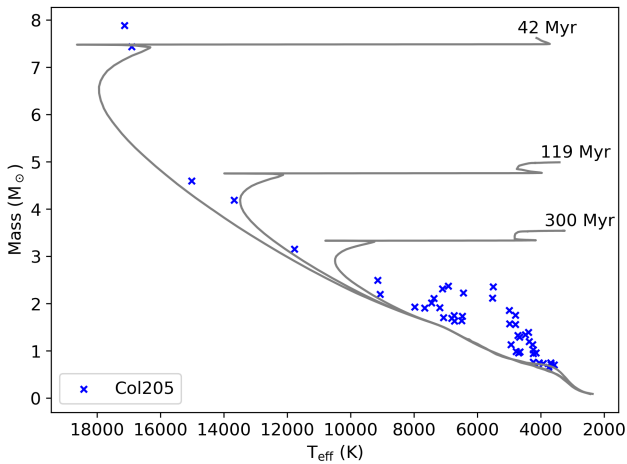


Figure 6. Individual stellar mass estimated in this work as a function of effective temperature obtained from *Gaia* DR3, compared with three isochrones from PARSEC models that illustrate the agreement of parameters obtained from different databases.

Part of the problem can be solved by enlarging the sample at least to counting with a similar number of members found in the published catalogues (see Table 1). For some clusters (Mrk38, NGC 2659, and NGC 6494), the counting of P_{50} members are close to the cataloged values. For the other clusters, we increased the list of considered members by choosing lower limits of membership probability. The adopted limit was $P = 31$ percent for Col205 and IC 2602, $P = 20$ percent for NGC 2168, and $P = 4.5$ percent for NGC 3532, which defined the sample containing the total number of stars that we consider as observed members (N_{obs}). These observed members were included in determining the individual mass based on the colour-magnitude diagram.

Observational bias due to *Gaia* detection limit must also be taken into account when discussing the sample completeness mainly for clusters at large distances (see Buckner et al. 2024, and references therein). We derived the mass function of the clusters to estimate the potential contribution of faint low-mass stars that may not have been detected by *Gaia*. The histogram of observed mass distribution was used in the fitting of the mass function $\xi(m) \propto m^{-(1+\chi)}$ adopted

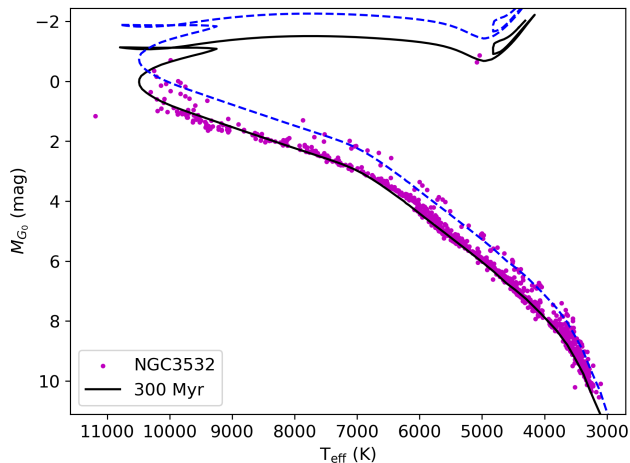


Figure 7. Distribution of absolute magnitude G as a function of effective temperature obtained from *Gaia* DR3 for the cluster NGC 3532 showing a dispersion due to the presence of binary stars. The PARSEC isochrone corresponding to the cluster age (full line) is also plotted with an offset of 0.75 mag (dashed line) to illustrate the good fitting of the binary population.

from Kroupa (2001). Following the method described by Santos-Silva & Gregorio-Hetem (2012), we use the slope of the observed mass distribution (χ given in Table 3) to obtain the number of lacking faint stars (N_{MF}), below the limit of detection. N_{MF} is estimated by integrating the Initial Mass Function suggested by Kroupa in the range of low-mass stars, assuming $\chi = 0.3 \pm 0.5$ for $m < 0.5 M_{\odot}$. Table 3 gives the total number of stars $N_{tot} = N_{obs} + N_{MF}$ and the total mass of the cluster $M_{tot} = M_{obs} + M_{MF}$, where M_{obs} is the sum of individual mass derived from the colour-magnitude diagram of the observed stars, and M_{MF} was estimated by integrating the mass function in the range of low masses.

4.5 Comparison with previous results

When increasing the lists of sources with more objects that have membership probability lower than 50 percent, the samples are comparable to the maximum number of members reported in the literature (see Table 1), showing completeness that varies from 72 percent to 100 percent for Col205, IC 2602, NGC 2168, NGC 3532. For the lists that remained with P_{50} members only, the number of objects is between the minimum and the maximum values reported in the literature, varying in the range of 42 - 60 percent of the maximum values, respectively, for NGC2659a and NGC6494. On the other hand, for Mrk38a, the list of P_{50} objects is 0.62 larger than the maximum value found in the literature.

Concerning the age estimation obtained from the isochrone fitting, which strongly depends on the massive and intermediate-mass stars, the inclusion of more objects (mainly low-mass stars) does not change the age obtained for the P_{50} members. Comparing the results given in Table 2 with those of Table 1, we find a good agreement (more than 0.75 of the maximum value from the literature) for the clusters IC 2602, Mrk38a, NGC 2659a, and NGC 3532. On the other hand, for NGC 2168 and NGC 6494, we found

ages more compatible with results from Dias et al. (2021) and Cantat-Gaudin et al. (2018b) that reported lower values when compared with Bossini et al. (2019). In the case of Col205, our estimation (42 Myr) is almost 5 times larger than the previous results.

As discussed in Sect. 6.1, an enlarged list of possible members ($P > 10$ percent) was analysed for NGC 2659a, but there was no change in the parameters that were determined for the constrained sample (P_{50} members). The main impact of the incompleteness is on the estimation of total mass (see Sect. 4.4). However, since the cluster mass is not provided in the public catalogues we analysed (Table 1), it cannot be compared with our derivations.

5 SPATIAL DISTRIBUTION

In the literature, several methods exploring the surface density distribution have been adopted to better understand the formation and evolution of substructures in the distribution of young stars, investigating if they are linked (or not) to the mass segregation in their original clouds. Recently, statistical tests have been performed to quantify the kinematic substructures of star-forming regions based on N -body simulations of artificial data points distributions (e.g. Blaylock-Squibbs et al. 2022; Arnold et al. 2022).

Different examples of works are found covering structures ranging from large-scale distributions to the smallest ones. For instance, Pouteau et al. (2023) used the ALMA 1.3 mm and 3 mm continuum images to investigate the relation of core distributions and mass segregation with the density and kinematics of the gas of star-forming clouds. In nearby clusters, such as NGC 1333, the method to estimate mass segregation was applied to investigate the distribution of very low-mass stars to understand the origin of planetary-mass stars (Parker & Alves de Oliveira 2023). Considering more distant regions, the estimation of parameters related to the fractal statistics have been explored for extragalactic objects, for instance, a large sample of star clusters of the Magellanic Clouds that were studied by numerical simulations (Daffern-Powell & Parker 2020) and based on observational VISCACHA data⁸ (Santos et al. 2020; Rodríguez et al. 2023).

Here, we infer the geometric structure of our sample by analysing the stars' spatial distribution that hints at how the stellar clustering's morphology evolves. This section is dedicated to the morphology diagnosis that uses the density profile fitting to estimate the size of the cluster and its core radius; the parameters related to the fractal statistics; local surface density, and mass segregation.

The methodology for fitting the surface density profile and calculating fractal parameters is adopted from HGH19, whose description is summarized below.

5.1 Cluster size and core radius

The mean values of equatorial coordinates and respective standard deviations ($\alpha \pm \sigma_{\alpha}, \delta \pm \sigma_{\delta}$) given in Table 2 roughly

⁸ VISCACHA: VIvisible Soar photometry of star Clusters in tApid and Coxi HuguA' Survey (Maia et al. 2019; Dias et al. 2020).

correspond to the center of the 2D projected spatial distribution of the cluster members. As indicated by the different values of σ_α and σ_δ , some clusters may display an elongated distribution, which area is better represented by a convex hull. Figure 8 shows an example of this geometric distribution that defines the minimal spanning tree (MST), the smallest network of lines connecting the set of data points without forming closed loops. The sum of the edge lengths in the MST is minimized, and the area of the convex hull contains all points projected on the cluster plane.

The cluster size was estimated using two different methods based on different lists of objects that provide minimum and maximum values for the cluster radius.

First, we studied only the distribution of the most probable members (P_{50}). Following the methodology proposed by Gower & Ross (1969), we constructed the MST adopting the algorithm from Kruskal (1956). The lower value for the radius (R_{P50}) given in Table 2 is defined by the radius of the circle having the same area as the convex hull. The standard deviation of R_{P50} was estimated using the Bootstrap method (Efron 1979).

A second method was adopted to estimate the total radius of the cluster (R_{tot}) that is achieved by fitting the density profile of the region containing the projected distribution of both cluster members and field stars. The observed density profile is determined by counting the number of stars as a function of their distance to the center of the cluster. We adopted the King-like radial density profile (RDP) model suggested by Bonatto & Bica (2009) that is adapted from the surface brightness profiles proposed by King (1962):

$$\sigma(r) = \sigma_{\text{bg}} + \frac{\sigma_0}{1 + \left(\frac{r}{r_c}\right)^2}, \quad (2)$$

where σ_0 is the density at the center of the cluster and σ_{bg} is the background density. The radius of the core (r_c) is derived from $\sigma(r_c) = \sigma_0/2$.

The Levenberg–Marquardt method (Press et al. 1992) was adopted for the RDP fitting based on maximum-likelihood statistics, with goodness-of-fitting function given by χ^2 .

The maximum value for the cluster radius (R_{tot}) is defined by the point where the cluster stellar density reaches the background density (see Table 3).

Based on the parameters derived from the RDP fitting, we also calculate the density-contrast (δ_c) parameter that quantifies how compact the cluster is. According to Bonatto & Bica (2009), this parameter is given by

$$\delta_c = 1 + \left(\frac{\sigma_0}{\sigma_{\text{bg}}}\right), \quad (3)$$

where compact clusters are expected to have $7 < \delta_c < 23$. Table 4 gives the values of density-contrast calculated for our clusters. According to this criterion, only NGC 2659a is considered compact.

5.2 Crossing time and dynamical age

The radius obtained from the fitting of the King’s profile corresponds to an area larger than the distribution of P_{50} members and possibly encompasses low-mass field stars. The same can be said about the estimation of M_{tot} that is considered an upper limit for the total mass of the cluster. Due

Table 3. Results from the fitting of the mass function and the radial density profile.

Cluster	N_{obs}	M_{obs} M_\odot	χ	N_{tot}	M_{tot} M_\odot	R_{tot} pc
Col205	108	218	1.12	943	1052±17	8.1±0.1
IC2602	317	199	0.54	326	232±20	9.1±0.4
Mrk38a	271	265	1.59	421	469±14	4.6±1.9
Mrk38b	75	76	-0.46	83	102±3	4.6±1.9
NGC2168	1281	1490	1.00	4173	4406±160	22.9±0.1
NGC2659a	98	140	-0.13	219	275±14	8.5±0.2
NGC2659b	96	174	-0.78	163	239±15	10.3±0.3
NGC3532	1847	1463	0.49	2151	2083±145	17.8±0.1
NGC6494	424	530	-0.39	554	713±47	7.5±0.1

to the differences in the lists of objects, we calculated two values for crossing time and dynamical age, giving a range of expected values. These ranges are presented in Table 4, where the first value corresponds to the calculation using the minimum estimation for mass and radius (M_{P50} , R_{P50}) and the second value is a result from the use of the maximum parameters (M_{tot} , R_{tot}).

Based on the mass M and radius R adopted for the cluster, we used the expression $T_{\text{cr}} = 10(R^3/GM)^{1/2}$ to estimate the crossing time. The ratio of cluster age to crossing time is used to quantify the dynamical age expressed by the parameter Π . According to Gieles & Portegies Zwart (2011), the expanding objects have $\Pi < 1$ and can be distinguished from bound star clusters with $\Pi > 1$.

Five objects of our sample show $\Pi < 1$ that corresponds to unbound clusters (Col205, IC 2602, Mrk38a, NGC 2168, and NGC 2659a), in agreement with previous results (HGH19). On the other side, the new results for NGC 3532 and NGC 6494 indicate $\Pi > 1$, leading to a new classification that suggests these are bound star clusters. As discussed in Sect. 7, the main difference from previous results is the larger number of members that are considered in the present work, which increased the total mass of the cluster, as well as the new isochrone fitting that gives an older age for these objects.

The range of Π values presented by Mark38b and NGC 2659b indicates they are unbound clusters. Since HGH19 did not individually analyse these subgroups, we compared them with their main companions. Both cases show considerable differences in dynamical age, suggesting that Mark38b and NGC 2659b are stellar groups respectively distinguished from Mrk38a and NGC 2659a.

5.3 Fractal statistics

The fact that most young clusters are found in a concentrated hierarchy of clusters within clusters makes their geometric distributions well-represented by fractals. In fractal star clusters, the level of substructures can be inferred using statistical analysis and measuring the Q -parameter for observed clusters or simulations of artificial data point distributions (see Delgado et al. 2013; Jaffa et al. 2017, for instance).

The method for determining the fractal parameters \bar{m} , \bar{s} , and Q was first proposed by Cartwright & Whitworth (2004), aiming to describe the geometrical structure of points distribution and statistically quantifies the substructures. Measurements on the MST allow us to obtain

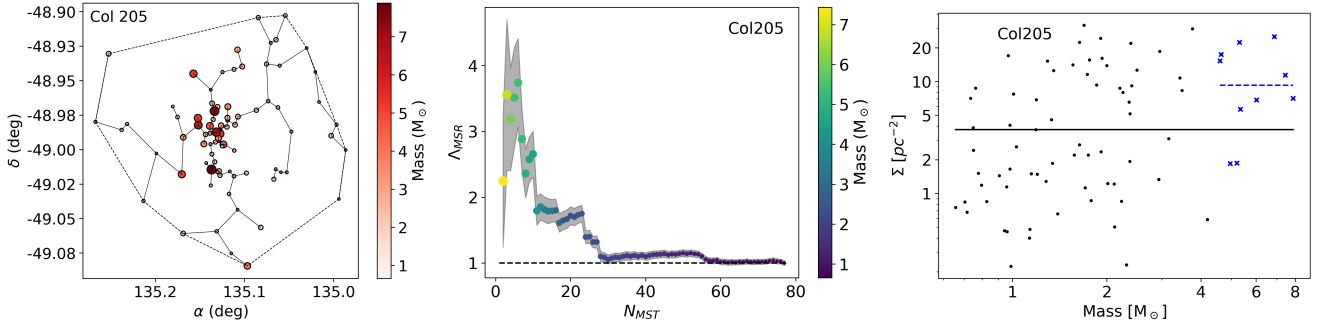


Figure 8. Results for Col205 from the analysis of surface density distribution. *Left:* Minimal spanning tree (MST) and convex hull area showing objects with different colours and symbol sizes according to their stellar mass. *Middle:* The mass segregation ratio Λ_{MSR} as a function of the number of stars N_{MST} . The occurrence of mass segregation is found above the limit $\Lambda_{\text{MSR}} = 1$ (dashed line). *Right:* The $\Sigma - m$ plot comparing the local surface density with the stellar mass. The full line shows Σ_{all} , the mean value obtained for all the cluster members, and a dashed line is used to indicate Σ_{10} that is estimated for the 10 most massive stars, which are denoted by blue \times .

Table 4. Results based on surface density distribution, crossing time, dynamical age, and fractal statistics.

Cluster	n pc^{-2}	r_c pc	δ_c	T_{cr} Myr	Π	\bar{m}	\bar{s}	\mathcal{Q}	Λ_{MSR}	Σ_{LDR}	p-value
Col205	9.5 ± 0.6	0.90 ± 0.08	4.63	67 – 105	0.6 – 0.4	0.67 ± 0.06	0.74 ± 0.05	0.90 ± 0.07	2.65 ± 0.35	2.48 ± 0.34	0.158
IC2602	20.8 ± 3.0	1.23 ± 0.37	3.75	248 – 270	0.5 – 0.4	0.62 ± 0.03	0.88 ± 0.03	0.70 ± 0.03	1.66 ± 0.23	2.16 ± 0.29	0.006
Mrk38a	7.6 ± 3.0	2.16 ± 1.87	1.26	22 – 69	0.9 – 0.3	0.69 ± 0.02	0.95 ± 0.02	0.73 ± 0.03	1.21 ± 0.15	1.30 ± 0.20	0.333
Mrk38b	7.6 ± 3.0	2.16 ± 1.87	1.26	49 – 147	5.0 – 1.7	0.78 ± 0.05	0.99 ± 0.03	0.79 ± 0.06	0.92 ± 0.10	0.85 ± 0.15	0.748
NGC2168	69.1 ± 1.7	1.74 ± 0.08	5.42	234 – 246	0.5 – 0.5	0.57 ± 0.02	0.55 ± 0.01	1.04 ± 0.03	2.05 ± 0.31	2.04 ± 0.37	0.090
NGC2659a	18.7 ± 3.5	0.95 ± 0.24	9.04	103 – 222	0.3 – 0.1	0.65 ± 0.05	0.71 ± 0.04	0.92 ± 0.06	1.95 ± 0.26	1.50 ± 0.24	0.229
NGC2659b	8.5 ± 9.7	0.37 ± 0.29	4.64	113 – 317	2.7 – 0.9	0.72 ± 0.05	0.83 ± 0.04	0.87 ± 0.05	1.21 ± 0.14	1.11 ± 0.20	0.646
NGC3532	162 ± 8	1.12 ± 0.12	3.09	74 – 249	4.1 – 1.2	0.64 ± 0.01	0.83 ± 0.01	0.77 ± 0.02	1.36 ± 0.18	1.60 ± 0.31	0.095
NGC6494	136 ± 20	0.24 ± 0.05	1.91	121 – 115	2.1 – 2.2	0.65 ± 0.02	0.77 ± 0.02	0.85 ± 0.03	2.11 ± 0.27	2.12 ± 0.33	0.030

$\mathcal{Q} = \frac{\bar{m}}{\bar{s}}$, where \bar{m} is the mean edge length that is related to the surface density of the points distribution, and \bar{s} is the mean separation of the points.

Generally, an initially fractal star-forming region is expected to evolve to become smoother and more centrally concentrated. However, different initial conditions or differences in establishing the borders of the considered region will cause significant changes in the position of the pair of parameters $\bar{m} - \bar{s}$ in a plot that is often used to separate smooth distributions from substructured regions (Daffern-Powell & Parker 2020).

Inferences of \bar{m} and \bar{s} depend on the total number of considered points N , which correspond in this work to the number of P_{50} members, and are normalised by A_N , the area of the convex hull (Schmeja & Klessen 2006).

These fractal parameters are useful to distinguishing fragmented ($\mathcal{Q} < 0.8$) from smooth distributions ($\mathcal{Q} > 0.8$), small-scale fractal subclustering can be quantitatively distinguished from distributions with large-scale radial clustering.

Table 4 gives the fractal parameters obtained for our sample, which are discussed in Sect. 6.2 based on the comparative analysis with previous results. In this case, the study considers the expected distribution in the $\bar{m} - \bar{s}$ plot indicating different types of structures, according to numerical simulations (Parker 2018).

Our new results better indicate the cluster type distribution, probably due to the larger number of members considered here compared to HGH19. The results are not well defined only in the case of NGC 2659b, but the value $\mathcal{Q} = 0.87$ indicates a radial concentration, while Mrk38a

($\mathcal{Q} = 0.73$) is near the homogeneous boundary between fractals and radial profiles.

An additional analysis of the cluster type distribution was performed by calculating the fractal dimension for the clusters that have $\mathcal{Q} < 0.8$. Following Canavesi & Hurtado (2020), for instance, we adopted a simple definition of the Box-Counting dimension from Feder (2013). In summary, this method considers several cubes ($N_{\delta(F)}$) in a $F \in \delta^n$ set with a δ size. If $N_{\delta(F)}$ intersects F , the box-counting dimension D_b is defined by the slope of $\log(N_{\delta(F)})$ versus $-\log(\delta)$. We found fractal box dimension $D_b > 2.6$ for IC 2602, Mrk38a, and NGC 3532, indicating they do not show high levels of substructures, tending to smooth distributions as expected for regions having fractal dimension $D \sim 3$. For Mrk38b, which has $\mathcal{Q} \sim 0.8$, the type of distribution remains undefined.

For clusters with $\mathcal{Q} > 0.8$, we adopted the radial distribution $n \propto r^{-\alpha}$ in order to estimate α through the fitting of star counts in intervals of radius $r + dr$ (Cartwright & Whitworth 2004). In this case, we found $1.2 < \alpha < 2.4$ corresponding to intermediary distributions, in between uniform density profile ($\alpha = 0$) and centrally concentrated distribution ($\alpha = 3$).

5.4 Distribution of massive stars

Analysing the properties of the massive star as a function of age, surface density, and structure is useful in order to understand better the origin and evolution of mass segregation

of stellar clusters (e.g. Dib et al. 2018; Maurya et al. 2020; Kim et al. 2021; Nony et al. 2021)

In this section, we discuss two forms to quantify if massive stars are concentrated (or not) in a projected distribution by calculating the mass segregation ratio (Λ_{MSR}) and plotting the local surface density (Σ) as a function of mass.

The parameter Λ_{MSR} (Allison et al. 2009) is used to determine if massive stars are closer to each other. It is defined by:

$$\Lambda_{\text{MSR}} = \frac{\langle l_{\text{average}} \rangle}{l_{\text{subset}}}, \quad (4)$$

where $\langle l_{\text{average}} \rangle$ is the average (median) length of the MST measured for sets of N_{MST} random stars, and l_{subset} is the same measure made for the subset of N_{MST} most massive stars. In this work, we use a subset of $N_{\text{MST}} = 10$. We adopted the standard deviation from the dispersion associated with the roughly Gaussian distribution around $\langle l_{\text{average}} \rangle$ to represent the uncertainty on the estimate of the mass segregation ratio. The cases of mass segregation are indicated by $\Lambda_{\text{MSR}} > 1$.

Another parameter to be considered is Σ_{LDR} , commonly used to indicate if the massive stars are in regions of higher surface density than those where low-mass stars are found. The calculation of the local stellar surface density (Maschberger & Clarke 2011) for an individual star i is expressed by:

$$\Sigma_i = \frac{N-1}{\pi r_{i,N}^2}, \quad (5)$$

where $r_{i,N}$ is the distance between a given star and its N^{th} nearest neighbour. In this work, we set $N = 10$. Following Parker et al. (2014), we adopted the local density ratio:

$$\Sigma_{\text{LDR}} = \frac{\tilde{\Sigma}_{\text{subset}}}{\tilde{\Sigma}_{\text{all}}}, \quad (6)$$

where $\tilde{\Sigma}_{\text{subset}}$ is the average measured for a given subset of stars, and $\tilde{\Sigma}_{\text{all}}$ corresponds to the average calculated for all the stars of the cluster. If the subset contains massive stars concentrated in dense regions, its local surface density is expected to be higher than the whole sample. In this case, the mass segregation is indicated by $\Sigma_{\text{LDR}} > 1$. With this method, it is possible to quantify if massive stars are found in dense regions, which is different from the mass segregation measured by Λ_{MSR} (Parker et al. 2014; Parker & Goodwin 2015).

Following the same method to infer the standard deviation of R_{P50} (see Sect. 5.1), the Σ_{LDR} uncertainties were estimated using the bootstrap technique (Efron 1979). The method creates a simulated data set considering a variation of each parameter (positions) within a confidence level corresponding to a given distribution. Then, the standard deviation of this set of values is calculated.

An example of the results of Λ_{MSR} and Σ compared with the mass distribution is shown in Fig. 8. The parameters related to the fractal statistics and the geometric structure of the clusters are given in Table 4. The resulting Σ_{LDR} , obtained from the ratio of the values corresponding to the horizontal lines in Fig. 8 (right panel) shows that our clusters tend not to have massive stars concentrated in regions of high surface density, which is indicated by $\Sigma_{\text{LDR}} \sim 1$.

Aiming to quantify the significance of the deviation from the median for all stars, we calculate the p-values using a Kolmogorov-Smirnov test for the cumulative distribution of the radial distances from the center of all stars and the 10 most massive stars. Following Parker & Goodwin (2015), we adopted a p-value < 0.1 as the significance threshold. If $\Sigma_{\text{LDR}} \sim 1$ and p-value > 0.1 , the distributions show no significant difference, indicating that the most massive stars are not mass segregated. This is confirmed for Mrk38a,b and NGC 2659a,b. However, Col205 and NGC 3532 are too close to the adopted threshold, making it difficult to gauge whether the differences are significant. On the other hand, for IC 2602, NGC 2168, and NGC 6494, the parameters $\Sigma_{\text{LDR}} > 2$ and p-value < 0.1 are clear signature of mass segregation.

In particular for NGC 6494, Tarricq et al. (2022) found mass segregation ratio $\Lambda_{\text{MST}} = 1.37$ that is lower than our result but still compatible (see Table 4 and Fig. B8).

6 COMPARATIVE ANALYSIS

6.1 Astrometric results

The mean values of position found for the cluster members (see Table 2) were compared with previous results from the literature (see Table 1) by calculating the offset on equatorial coordinates (α , δ) with respect the values obtained in this work. The conversion of angular measurements to linear dimensions, which gives Δ_{pos} (position offset in parsec), was made using the mean value of the distance mode.

The comparison of proper motion was made by calculating the offset of tangential velocity $\Delta\mu = (\Delta\mu_{\alpha}^2 + \Delta\mu_{\delta}^2)^{0.5}$, given in mas yr^{-1} that was converted into km s^{-1} in the same way we used for the position offset.

In the case of double clusters, we adopted the results for Mrk38a and NGC 2659a as a reference, meaning that these main groups and the single clusters present offset equal zero in this comparative analysis.

The estimated ranges quantifying the differences and similarities between our results and those in the literature are shown in Table 5. The table provides the minimum and maximum values of position and velocity offsets, along with their respective references. Figure 9 displays the offsets Δ_{pos} and $\Delta\mu$ for the entire sample compared with the literature, identifying individual works by coloured bars.

First, we discuss the single clusters. Compared with our new results, the offsets are very low, excepting the comparison with Cantat-Gaudin et al. (2018a) data (green bars) for NGC 2168 and NGC 6494, which are based on UCAC4⁹. A possible explanation for these higher velocity offsets is the difference in the proper motion used from a different database, which in some cases may present larger uncertainties when compared with the *Gaia* data. Another possible cause of discrepancies between our results and the literature is related to different estimates of the cluster distance. This problem is avoided in the left panel of Fig. 9 that displays Δ_{pos} as a function of $\Delta\mu$, both given in angular measurements. Again, the points showing large offset in velocity are

⁹ The fourth U.S. Naval Observatory CCD Astrograph Catalogue.

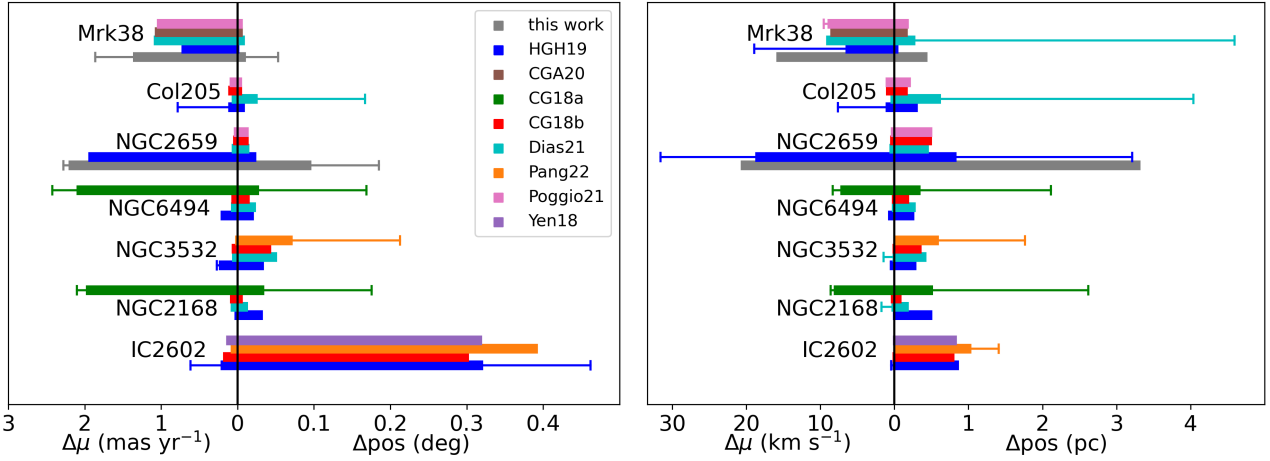


Figure 9. The spatial distribution and velocities estimated in this work compared with the literature. The uncertainties are represented by error bars corresponding to the largest error or offset found for each cluster. *Left:* The coloured bars indicate different works (see Table 1) and the offsets of their respective values on the position (Δpos) and tangential velocity ($\Delta\mu$), given in angular units. In the case of double clusters, the grey bars represent the offset of results for the secondary group (Mrk38b and NGC 2659b), respectively, to the main clusters (Mrk38a and NGC 2659a), which were adopted as referential. *Right:* The same as left panel, with offsets given in linear units.

Table 5. Comparison of our results with the literature.

Cluster	Δpos (deg)	Δpos (pc)	$\Delta\mu$ mas yr ⁻¹	$\Delta\mu$ km s ⁻¹
Col205	0.009 ^c 0.025 ^d	0.17 ^e 0.62 ^d	0.06 ^d 0.11 ^e	0.43 ^d 1.1 ^{cef}
IC2602	0.302 ^e 0.392 ^g	0.80 ^e 1.03 ^g	0.08 ^g 0.21 ^c	0.06 ^g 0.15 ^c
Mrk38a	0.001 ^c 0.010 ^b	0.05 ^c 0.51 ^b	0.72 ^c 1.36 ^b	6.5 ^c 18.3 ^b
NGC2168	0.006 ^e 0.034 ⁱ	0.09 ^e 0.51 ⁱ	0.03 ^c 1.98 ⁱ	0.12 ^c 8.0 ⁱ
NGC2659a	0.014 ^{ef} 0.095 ^b	0.45 ^d 3.31 ^b	0.04 ^f 2.20 ^b	0.39 ^f 20.7 ^b
NGC3532	0.034 ^c 0.071 ^g	0.29 ^c 0.59 ^g	0.02 ^g 0.24 ^c	0.05 ^g 0.54 ^c
NGC6494	0.015 ^e 0.027 ⁱ	0.19 ^e 0.34 ⁱ	0.07 ^e 2.09 ⁱ	0.24 ^{de} 7.2 ⁱ

Notes: For each cluster, the minimum and maximum offsets are in the top and bottom lines, respectively. (b) Secondary cluster in this work; (c) HGH19; (d) Dias et al. (2021); (e) Cantat-Gaudin et al. (2018b); (f) Poggio et al. (2021); (g) Pang et al. (2022); (h) Yen et al. (2018); (i) Cantat-Gaudin et al. (2018a).

NGC 2168 and NGC 6494, due to the values adopted from UCAC4.

Proceeding with the same evaluation for double clusters, we found larger discrepancies than expected. For Mrk38, the separation is larger on proper motion. On the other hand, the position we found for Mrk38a is in good agreement with the literature, while Mrk38b shows negligible Δpos in comparison with its pair, corresponding to minimal differences on the projected distribution.

Noticeable discrepancies are also found for NGC 2659 compared with HGH19, which results are roughly in between the values obtained for both groups in the present work, mainly for NGC2659b that has the largest distance from its

pair. The discrepancies of both components of NGC 2659 in comparison with HGH19 indicate that our previous results were obtained from a mixing of members of both groups. It can be also noted that our present results for NGC 2659a are in better agreement with literature (Dias et al. 2021; Cantat-Gaudin et al. 2018b; Bossini et al. 2019).

We have checked the possible coincidence of NGC 2659b with other open clusters (OCs) previously suggested as part of the same group. Figure 10 compares results only for NGC 2659 and other OCs that could have similar properties. These OCs were reported in the literature as candidates to possible companions of NGC 2659, which could constitute a double or multiple cluster. This plot shows the offsets in position as a function of differences in cluster distance (Δdist) when compared with our present results. In this case, offsets with positive values indicate more distant objects (background), while negative values are used for lower distances (foreground). The symbols have different colours representing the offset of tangential velocity. The blue symbols indicate similarity in velocity compared with NGC2659a, as it is noted for the results from the literature (shown by blue squares Dias et al. 2021; Cantat-Gaudin et al. 2018b; Bossini et al. 2019), while red symbols correspond to velocities similar to the results for NGC2659b ($\Delta\mu > 2$ mas yr⁻¹, where \star indicates this work, and the red square is from HGH19).

The OCs (e.g. Liu & Pang 2019; Casado 2021) are represented by blue circles indicating similarity in velocity compared with NGC2659a. However, three of them have larger distances ($\Delta\text{dist} > 100$ pc): Gull5, UBC 482, and Cas61. Other five OCs have lower distances ($\Delta\text{dist} < 70$ pc): LP58; Pismis 8; SAI92; Rupr71; and NGC2645. The last candidate, Cas28, has projected position larger than 1 degree in the sky, which is also observed for all the other clusters. Due to these large discrepancies, it is more conservative not considering they belong to the same group.

Finally, UBC 246, also named Pismis 9, was suggested to form a pair with NGC 2659a (Giorgi et al. 2023), which has a projected position and tangential velocity similar to

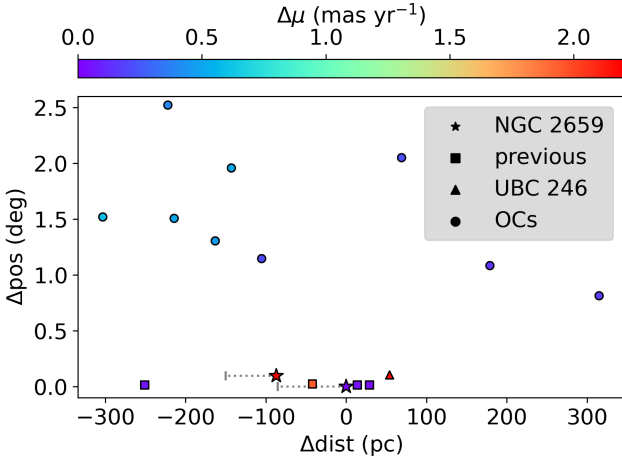


Figure 10. The offsets in position and velocity for NGC 2659a (blue \star) and NGC 2659b (red \star), compared with previous results from literature, and other open clusters (OCs) suggested to be companions groups, such as UBC 246, for instance. The grey dotted lines show the distance offset obtained for a larger sample that includes additional members ($P < 50$ percent)

NGC2659b. However, its distance is larger at more than 150 pc (e.g. Cantat-Gaudin et al. 2020; Poggio et al. 2021). Even when considering the uncertainty in estimation, the extent of their separation remains too significant to align with the same subgroup. It must be kept in mind that our selection of 96 members is more restrictive than other works that consider samples with at least three times more objects scattered around the mean spatial position, which naturally span in larger ranges of distances. To be more conclusive about the similarities and differences between NGC 2659b and UBC 246, it is necessary to include additional objects, candidates showing membership lower than 50 percent, to have the same basis of comparison with other works.

Poggio et al. (2021) reported a list of 270 members for UBC 246. To achieve a similar sample, for NGC 2659b, we selected the objects that have membership probability $P > 0.1$ percent and fractional parallax uncertainty $f < 0.5$. The mean values (and respective standard deviation)¹⁰ for this enlarged sample are in good agreement with the literature for UBC 246 (mainly Poggio et al. 2021), except for the slightly different distance: $d = 2120$ pc (Cantat-Gaudin et al. 2020) or $d = 2025$ pc (Tarricq et al. 2022), but still within the uncertainties. This confirms that NGC 2659b is indeed the same cluster previously cataloged as UBC 246.

When comparing NGC 2659b with NGC 2659a (using a sample of 154 objects that have $P > 10$ percent, $f < 0.5$), the differences between the mean values for each parameter (presented above) remain comparable with those obtained for the samples restricted to P_{50} members. The new results show less than 0.5 percent for differences in position and proper motion, while the standard deviations, as expected, are almost 50 percent larger than the previous results (P_{50}

¹⁰ $(\alpha, \delta) = (130.712(0.006), -44.935(0.054))$ deg, $\varpi = 0.509(0.052)$ mas, $\mu_{\alpha^*} = -4.379(0.101)$ mas yr⁻¹, $\mu_{\delta} = 3.015(0.134)$ mas yr⁻¹, $d = 1916(218)$ pc.

members). The main difference, but not significant, occurs for the new values of distance mode, which change the offset from $\Delta\text{dist} = 2066 - 1979 = 87$ pc (measured for samples of P_{50} members) to $\Delta\text{dist} = 1980 - 1916 = 64$ pc. An illustration of these differences is shown by dotted lines linked to the star points representing NGC 2659a,b in Fig. 10. These results indicate that enlarging the sample (by a factor of ~ 3 in the case of NGC2659b) does not give different parameters that were found for the list of the most probable members. Despite the similarity in the projected distribution of both groups, NGC 2659b tends to be in a region more than 0.05 deg to the NE away from NGC 2659a. There is a difference of more than 50 pc in distances, where NGC 2659b is in the foreground, and significant differences in proper motion and age confirm that this cluster is not a subgroup of NGC 2659a.

6.2 Structure

The early evolution of star clusters and their original structure can be explored by comparing the fractal parameters obtained from the observed surface density distribution with theoretical simulations. In a recent study of the NGC 2264 star-forming region, Parker & Schoettler (2022) used the \mathcal{Q} -parameter to quantify the spatial distribution of stars for two subclusters centered around the stars S Mon and IRS 1/2. Both groups have $\mathcal{Q} \sim 0.8$, meaning they have neither a substructured nor a centrally concentrated distribution. According to different age estimates in the literature, the star formation activity seems to have started first in the S Mon region (~ 5 Myr) and more recently (~ 2 Myr) for the group IRS 1/2 (e.g. Schoettler et al. 2022). This is one example of studies using the \mathcal{Q} -parameter, comparing it with the mass segregation ratio and the local density, similar to the analysis performed in the present work.

Here, we aim to investigate the variation in the fractal parameters if single or multiple structures are considered in the distribution of our cluster sample. Figure 11 shows the locus of different regions defined by numerical simulations from Parker (2018) using convex hull area normalization for synthetic star-forming regions that contain 300 points. We adapted ellipses covering the span of points from the results for each adopted geometry (fractal dimension or radial density profile) to display the loci of six parameters used in the simulations (see original distributions of points in Fig. A3(b) from Parker 2018). Overimposed on these ellipses, we plot the values of \bar{m} and \bar{s} obtained in this work compared with previous results from HGH19. Above the line of $\mathcal{Q} = 0.8$ is found the loci of simulations with RDP described by $n \propto r^{-\alpha}$, where $\alpha = 0$ indicates uniform density profile, while $\alpha = 2.9$ corresponds to centrally concentrated distributions. On the other hand, the regions with $\mathcal{Q} < 0.8$ correspond to simulations that adopt geometries varying from very substructured fractal (fractal dimension $D = 1.6$) to smoother distributions ($D = 3$).

It can be noted in Fig. 11 the improvement we obtained in the accuracy of the fractal parameters, probably due to the larger number of members considered in this work for most of our clusters, compared with previous results (HGH19). This means that the position of the clusters in the $\bar{m} - \bar{s}$ plot coincides with well-defined regions representing RDP distributions in the case of Col205, NGC 6494 (α

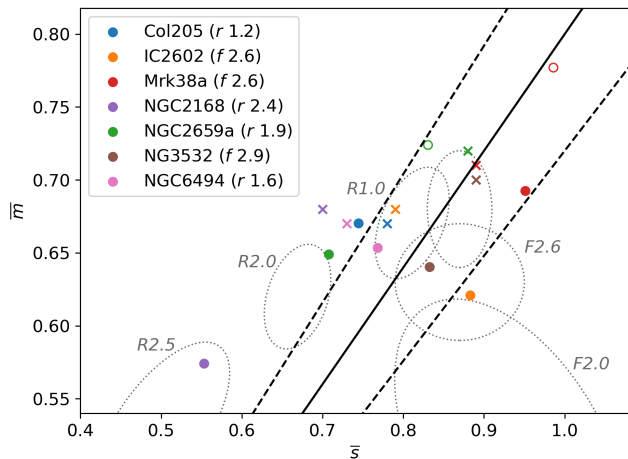


Figure 11. Plot of \bar{m} and \bar{s} comparing results from HGHI9 (shown by \times) with those obtained here (circles, with open symbols in the case of Mrk 38b and NGC 2659b). The full line indicates $\mathcal{Q} = 0.8$, with 10 percent deviation (dashed lines). The dotted ellipses show the simulations by Parker (2018) defining the locus of regions with radial distributions (from R0 to R2.5) or fractals (F2.0, F2.6, and F3.0). In both types of structure, the smooth distributions (R0 and F3.0) coincide in the same area (unlabeled ellipse). Results from our estimation of fractal dimension (f) or slope of radial profile (r) are indicated in the figure’s legend.

$= 1$), NGC 2659a ($\alpha = 2$), and NGC 2168 ($\alpha = 2.5$). On the other hand, IC 2602 and NGC 3532 have $\mathcal{Q} < 0.8$, coinciding with the simulated fractal region F2.6. As discussed in Sect. 5.3, the legend of Fig. 11 also shows the results from calculating the fractal box-dimension (D_b) or the slope (α) of the RDP, respectively labeled by “f” or “r” aiming to compare with the simulated regions directly.

A last diagnosis of our analysis is obtained from the plots of the \mathcal{Q} -parameter against the mass segregation ratio and the local density shown in Fig. 12. In these plots, the areas corresponding to the N-body simulations from Parker & Schoettler (2022) are displayed, representing results for a highly substructured star-forming region under subvirial¹¹ initial conditions. Previous results (HGHI9) are also plotted for comparison, with principal differences noted for Λ_{MSR} tending to be larger in the present work. Σ_{LDR} seems to show lower values, but for all the objects of our sample, both parameters remain in the 1.0 to 2.5 range. These values coincide with the interval expected by the simulations corresponding to the early evolution of the clusters (age = 2 and 5 Myr) but do not reach the maximum values found by Parker & Schoettler (2022) for these adopted initial conditions. No significant changes were noted in the \mathcal{Q} range, since our sample coincides with the range expected by the simulations, except for Mrk38b, which shows inverse mass segregation.

Comparing \mathcal{Q} , Λ_{MSR} and Σ_{LDR} obtained from simulations for the initial conditions adopted by Parker & Schoettler (2022), it can be concluded that the dynamical evolution erases the initial structure (see in Fig. 12 the area

¹¹ $\alpha_{\text{vir}} = 0.3$, where α_{vir} is the ratio of potential energy to kinetic energy.

corresponding to the distribution of points at 0 Myr). After 2 Myr, their levels of substructure decrease significantly, and their levels of mass segregation increase. Although the ages of our sample are much older, their values of \mathcal{Q} and mass segregation suggest that most of our clusters would be consistent with those initial conditions. However, as discussed in HGHI9, they would also be consistent with other conditions. For instance, we also compare our results with simulations of synthetic regions from Parker et al. (2014) using $\alpha_{\text{vir}} = 1.5$ and $D = 3$. Fig. 12 shows a shaded area corresponding to the smoothed span of the points resulting from these simulations at three ages (0, 2 and 5 Myr). In this case, the choice of initial conditions is related to the simulated distribution of points coinciding with the same range of parameters found for our clusters.

7 DISCUSSION

We selected seven OCs from a sample previously studied by us to investigate the possible presence of double- or multiple structures. The choice of the objects was based on the large dispersion of their ages, which were estimated by using near-infrared photometry (HGHI9). In the present work, the characterization of the cluster members was revisited in the light of *Gaia* DR3 astrometric and photometric data that allowed a significant increase in the list of studied stars, corresponding to a more complete population when compared with our previous results. Near- to mid-infrared data and visual extinction maps were used to inspect the circumstellar and interstellar environments that could be related to dust emission from a protoplanetary disc or the presence of a surrounding molecular cloud. However, our sample does not show large amounts of dust emission, considering that only a few members of the younger clusters seem to be disc-bearing stars, and the A_V levels in the direction of the clusters are lower than 1 mag for most of them.

We considered members of the clusters the stars with a membership larger than 50 percent (P_{50}), estimated by fitting a Probability Distribution Function to the observed proper motion. Only members presenting low fractional uncertainty of parallax ($f < 0.3$) were used to estimate the mean values of the astrometric parameters, as well as in the calculation of the most probable distance of the cluster that is determined from the distribution of the distance mode of the members. In total, we analysed 9 stellar groups, five of which are single clusters: Col205, IC 2602, NGC 2168, NGC 3532, and NGC 6494, which do not show any subgroup in their spatial distribution neither in proper motion. The other four groups are related to two candidates that possibly are pairs of clusters Mrk 38a,b and NGC 2659a,b, whose components are mainly distinguished when comparing the proper motion and the distance of the subgroups, while their position overlaps in the same projected region.

The colour-magnitude diagram constructed with the *Gaia* photometry was corrected from reddening using the extinction automatically estimated by the code Aeneas of the GSP-Phot package. For the *Gaia* sources lacking this correction, we have adopted a mean value of $E(B-V)$ that agrees with the A_V maps and provides a good fit for the isochrone corresponding to the cluster age. Individual stellar masses, determined from interpolation between evolutive

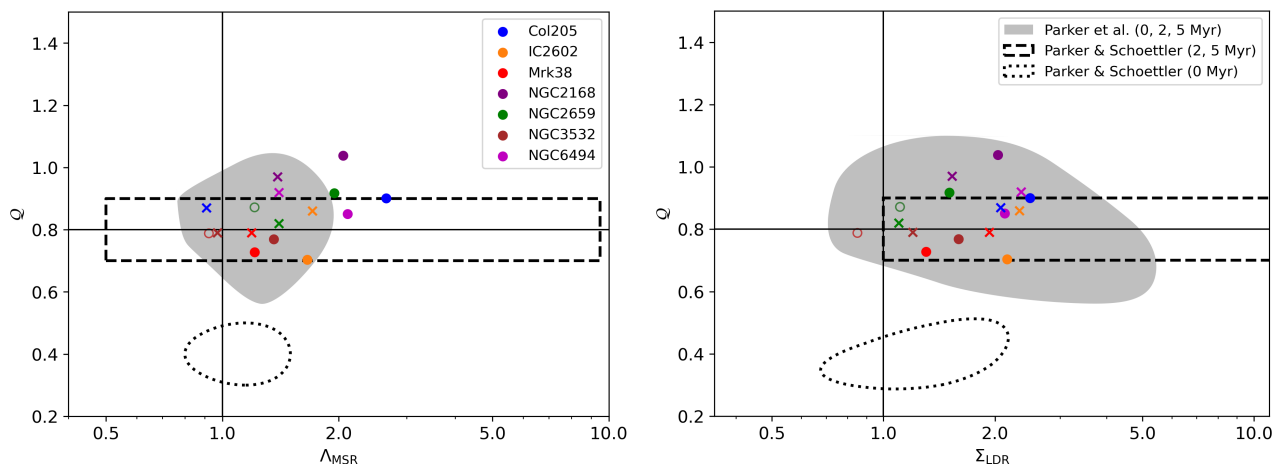


Figure 12. Comparison of Q with mass segregation ratio (left panel) and local surface density ratio (right panel). The legends are the same for both panels. Results from HGH19 are shown by \times , and open circles indicate the secondary group of double clusters. The highlighted areas represent smoothed distributions of points from N-body simulations of star-forming regions under different initial conditions. The hatched grey area shows simulations from Parker et al. (2014), and the areas delimited by dotted or dashed lines roughly correspond to the points distribution obtained by Parker & Schoettler (2022), which reaches up to $\Sigma_{LDR} \sim 40$ (not shown in the plot).

tracks, were compared with the effective temperature, confirming that the mass estimates are reliable mass. A comparison of the astrometric results with the literature was performed by measuring offsets in position (Δ_{pos}) and proper motion calculated in the form of tangential velocity ($\Delta\mu$), where our present results were adopted as references (that means zero points). We found low values for these offsets in the case of the single clusters that show $\Delta_{pos} < 1$ pc and $\Delta\mu < 1$ km s $^{-1}$ suggesting an excellent agreement with the literature.

The surface stellar distribution of subgroup Mrk38b entirely coincides with the main cluster Mrk 38a ($\Delta_{pos} \sim 0.1$ deg), but the offset on proper motion corresponds to more than 10 km s $^{-1}$. This subgroup is about 500 pc more distant than the distance we found for the main cluster. These differences suggest Mrk38b is a distinguished stellar group, which is older (250 Myr) and more scarce ($n = 2.4$ stars pc $^{-2}$) than Mrk38a (age= 30 Myr, $n = 14$ pc $^{-2}$) that is the main group previously known as a single cluster. Due to unusual nature of Mrk38b, as a second cluster in the direct line of sight, we examined the possibility that it is instead an asterism caused by a combination of the Gaia missions limited ability to detect (fainter) stars more distant than Mrk38b and/or large parallax uncertainties of identified members. We performed a test of eliminating sources with a parallax uncertainty $f > 0.2$ and re-calculated the membership probabilities. In this case, the number of sources is insufficient for the algorithm to discern two groups. Only one group is found, showing an elongated distribution in the considered parameter space. However, through visual inspection, it is still possible to identify a few members coinciding with the ranges of proper motion and parallax found for Mrk38b.

The largest offsets are found for NGC 2659b, separated from the main cluster by 3.3 pc and tangential velocity offset > 20 km s $^{-1}$. In Fig. 9 (right panel), we compared the main cluster NGC 2659a with other OCs from the literature that were suggested to be part of the same group due to their similar proper motion. However, all of these OCs

have shown large differences in distance (> 100 pc) or projected position (> 1 degree), which are too distant from each other to be considered components of the same stellar group. NGC2659b shows differences that indicate it is not a sub-structure of NGC 2659a. NGC 2659b has projected position and proper motion coinciding with the cluster UBC 246, but the distance we estimated is lower than the results from the literature.

The calculation of the structural parameters was based on the surface density distribution by constructing the MST that is used to estimate the size of the cluster and fractal parameters, which were compared with N-body simulations from the literature. For instance, the $\bar{m} - \bar{s}$ plot (see Fig. 11) indicates that clusters with $Q > 0.8$ (corresponding to radial distribution): Col 205, NGC 2168, NGC 2659a, and NGC 6494 occupy the areas coinciding with simulations that define the locus of centrally concentrated regions ($R = 1$ to 2.5). NGC 2659b also has $Q > 0.8$, but its \bar{m} and \bar{s} parameters do not coincide with the loci predicted by the simulations, just appearing near the region of smooth uniform distribution ($R=0$). Only IC 2602 and NGC 3532 do not show radial distribution, but low levels of substructures are found since they coincide with simulated fractal regions ($F=2.6$). Mrk38a and Mrk38b appear out of the simulated regions, but Mrk38a ($Q < 0.8$) seems to be tending to the region of smooth fractal distribution ($F=3$), while Mrk38b ($Q \sim 0.8$) has undefined distribution. These results are consistent with those calculated in Sect. 5.3.

The total mass of the clusters was used to estimate the crossing time and the dynamical age (Π) that indicates if the cluster is gravitationally bound. Half of our clusters are considered unbound since they have $\Pi < 1$. A possible exception is Mrk38a, which has $\Pi \sim 1$ and could be a bound young cluster whose age is near its crossing time. Larger values of dynamical ages were found for the oldest clusters of our sample: Mrk38b, NGC2659b, NGC 3532, and NGC 6494. There is a $\Lambda_{MSR} > 1$ trend for most of the clusters, except for the subgroup Mrk38b. However, the mass segregation is

only evident for half of the sample, which has $\Lambda_{\text{MSR}} \gtrsim 2$. The other clusters are consistent with $\Lambda_{\text{MSR}} \sim 1$ (within the errors). On the other hand, based on the values of $\Sigma_{\text{LDR}} \sim 1$ we conclude that massive stars tend not to be concentrated in regions of high surface density for most of our clusters, excepting IC 2602 and NGC 6530 that show mass segregation signature ($\Sigma_{\text{LDR}} > 2$ and p-value < 0.1).

The diagram comparing the mass segregation parameters as a function of Q also displays the results from N-body simulations considering different initial conditions. These simulations indicate the data points' distribution during the artificial clusters' early evolution. The plots in Fig. 12 show that most of our clusters present the same distribution found for simulations at 2 and 5 Myr. Only Col205, NGC 2168, and NGC2659a appear out of the areas predicted by the simulations. Their high values of Q indicate central concentration that is confirmed by their position in the $\overline{m} - \bar{s}$ plot tending to RDP distributions (R2 to R2.5 regions in Fig. 11). The comparison with the simulations (highlighted areas in Fig. 12) indicates that most of our clusters tend to smooth distribution ($Q \sim 0.8$) or a radial concentration ($Q > 0.8$) as they are evolving. One possibility is that these clusters could have lost their original substructures if they had been formed in highly substructured regions. Or, on the contrary, they retained their original geometry that possibly had low levels of substructures.

ACKNOWLEDGEMENTS

We warmly thank Professor Vera Jatenco-Pereira for the valuable suggestions on the text of this manuscript. We thank the anonymous referee for the constructive comments and suggestions. We acknowledge support from FAPESP (2020/15245-2; 2023/08726-2). This work has made use of data from the European Space Agency (ESA) mission *Gaia* (<https://www.cosmos.esa.int/gaia>), processed by the *Gaia* Data Processing and Analysis Consortium (DPAC, <https://www.cosmos.esa.int/web/gaia/dpac/consortium>). Funding for the DPAC has been provided by national institutions, in particular the institutions participating in the *Gaia* Multilateral Agreement. This research has made use of the SIMBAD astronomical database (Wenger et al. 2000), and the VizieR catalogue access tool (Ochsenbein et al. 2000, DOI : 10.26093/cds/vizieR) operated at CDS, Strasbourg, France. This publication makes use data products from the Two Micron All Sky Survey, which is a joint project of the University of Massachusetts and the Infrared Processing and Analysis Center/California Institute of Technology, funded by the National Aeronautics and Space Administration and the National Science Foundation. This publication makes use of data products from the Wide-field Infrared Survey Explorer, which is a joint project of the University of California, Los Angeles, and the Jet Propulsion Laboratory/California Institute of Technology, funded by the National Aeronautics and Space Administration.

DATA AVAILABILITY

The data underlying this article are available in machine-readable form at the CDS (VizieR On-line Data Catalogue), which correspond to the tables containing individual members' parameters and results.

REFERENCES

- Allison R. J., Goodwin S. P., Parker R. J. et al., 2009, *MNRAS*, 395, 1449
- Arnold B., Wright N. J., Parker R. J., 2022, *MNRAS*, 515, 2266
- Bailer-Jones C. A. L., 2015, *PASP*, 127, 994
- Blaylock-Squibbs G. A., Parker R. J., Buckner A. S. M., Güdel M., 2022, *MNRAS*, 510, 2864
- Bica E., Pavani D. B., Bonatto C., Lima E. F., 2019, *AJ*, 157, 12
- Bonatto C., & Bica E., 2009, *MNRAS*, 397, 1915
- Bossini D., Vallenari A., Bragaglia A. et al., 2019, *A&A*, 623, A108
- Bragaglia A., Alfaro E. J., Flaccomio E. et al., 2022, *A&A*, 659, A200
- Bravi L., Zari E., Sacco G. G. et al., 2018, *A&A*, 615, A37.
- Bressan A., Marigo P., Girardi L., Salasnich B., Dal Cero C., Rubele S., Nanni A., 2012, *MNRAS*, 427, 127
- Buckner A. S. M. et al., 2019, *A&A*, 622, A184
- Buckner A. S. M. et al., 2020, *A&A*, 636, A80
- Buckner A. S. M., Khorrami, Z., González M., Lumsden S. L., Clark P., Moraux E., 2022b, *A&A*, 659, A72
- Buckner A. S. M., Naylor T., Dobbs C. L., Rieder, S., Bending T. J. R., 2024, *MNRAS*, 527, 5448
- Canavesi, T., & Hurtado, S., 2020, *BAAA Vol. 61B*,
- Cantat-Gaudin T., Anders F., 2020, *A&A*, 633, A99
- Cantat-Gaudin T., Vallenari A., Sordo R. et al., 2018a, *A&A*, 615, A49
- Cantat-Gaudin T., Jordi C., Vallenari A. et al., 2018b, *A&A*, 618, A93
- Cantat-Gaudin T., Anders F., Castro-Ginardi A. et al., 2020, *A&A*, 640, A1
- Cardelli J. A., Clayton G. C., Mathis J. S., 1989, *ApJ*, 345, 245
- Cartwright A., Whitworth A. P., 2004, *MNRAS*, 348, 589
- Casado J., 2021, *Astronomy Reports*, 65, 755
- Casagrande L., Vandenberg D. A., 2018, *MNRAS*, 479, L102
- Cordoni G., Milone A. P., Marino A. F. et al., 2023, *A&A*, 672, A29
- Cutri R.M., Wright E.L., van Dyk, S. et al., 2003, *VizieR Online Data Catalog II/246: 2MASS All-Sky Catalog of Point Sources*
- Cutri, R. M., Wright, E L., Conrow, T. et al., 2013, *VizieR Online Data Catalog II/328: AllWISE Data Release*, originally published in: *IPAC/Caltech*.
- Daffern-Powell E.C., Parker R. J., 2020, *MNRAS*, 493, 4925
- Davidge T. J., 2017, *ApJ*, 837, 178
- Delgado A. J., Djupvik A. A., Costado M. T., Alfaro E. J., 2013, *MNRAS*, 435, 429
- Dias W.S., Monteiro H., Caetano T. C., Lépine J. R. D., Assafin M., Oliveira, A. F., 2014, *A&A*, 564, 79
- Dias W. S., Monteiro H., Moitinh, A., Lépine J.R.D., Carraro G., Pauzen E., Alessi B., Vilella L., 2021, *MNRAS*, 504, 356
- Dias B. et al., 2020, in Bragaglia A., Davies M., Sills A., Vesperini E., eds, *Proceedings of the International Astronomical Union, Volume 14, Symposium S351: Star Clusters: From the Milky Way to the Early Universe*, Vol. 14. p. 89–92, doi:10.1017/S174392131900694X
- Dib S., Schmeja S., Parker R., 2018, *MNRAS*, 473, 849
- Dobashi K., Uehara H., Kandori R. et al., 2005, *PASJ*, 57, S1
- Dobashi K., 2011, *PASJ*, 63, S1-S362

- Dobbie P. D., Napiwotzki R., Burleigh M. R. et al., 2009, *MNRAS*, 395, 2248
- Donada J., Anders F., Jordi C. et al., 2023, *A&A*, 675, A89
- Efron B., 1979, *Bootstrap Methods: Another Look At the Jack-knife*, *The Annals of Statistics* 7, 1-26
- Elmegreen B. G., 2008, *A&A*, 672, 1006
- Elmegreen B. G., 2018, *A&A*, 853, 88
- Fedele D., van den Ancker M. E., Henning Th. et al., 2010, *A&A*, 510, A72
- Feder J., 2013, *Fractals*, Springer Science & Business Media
- Fernandes B., Montmerle T., Santos-Silva T., Gregorio-Hetem J., 2019, *A&A*, 628, A44
- Fűrész G., Hartmann L. W., Szentgyorgyi A. H. et al., 2006, *ApJ*, 648, 1090
- Gaia Collaboration, Babusiaux C., van Leeuwen F., Barstow, M. A., et al., 2018b, *A&A* 616, A10
- Gaia Collaboration, Vallenari A., Brown, A. G. A., Prusti T. et al., 2023, *A&A*, 674, A1
- Gieles M., Portegies Zwart S. F., 2011, *MNRAS*, 410, L6
- Giorgi E. E., Pera M. S., Perren G. I. et al., 2023, *Boletín de la Asociación Argentina de Astronomía*, 64, 90
- González M., Alfaro E. J., 2017, *MNRAS*, 465, 1889
- González M., Joncour I.; Buckner A. S. M. et al., 2021, *A&A*, 647, A14
- Gouliermis D. A., Hony S., Klessen R. S., 2014, *MNRAS*, 439, 3775
- Gower J.C., Ross G.J.S., 1969, *Appl. Stat.*, 18, 54
- Gregorio-Hetem J., 2008, *The Canis Major Star Forming Region, Handbook of Star Forming Regions, Volume II: The Southern Sky ASP Monograph Publications, Vol. 5. Edited by Bo Reipurth, p.1, ISBN: 978-58381-671-4*
- Gregorio-Hetem J., Lefloch B., Hetem A. et al., 2021, *A&A*, 654, A150
- Hernández J., Hartmann L., Calvet N. et al., 2008, *ApJ*, 686, 1195
- Hetem A., Gregorio-Hetem J., 2019, *MNRAS*, 490, 2521
- Hu Q., Zhang Y., Esamdin A., Liu J., Zheng X., 2021a, *ApJ*, 912, 5
- Hu Q., Zhang Y., Esamdin A., 2021b, *A&A*, 656, A49
- Jackson R. J., Jeffries R. D., Wright N. J. et al., 2022, *MNRAS*, 509, 1664
- Jadhav, V. V., Roy K., Joshi N., Subramaniam A., 2021, *AJ*, 162, 264
- Jaffa S.E., Whitworth A.P., Lomax O., 2017, *MNRAS*, 466, 1082
- Kharchenko N.V., Piskunov A. E., Roeser S. et al., 2005, *A&A*, 438, 1163
- Kim S., Lim B., Bessell M. S. et al., 2021, *AJ*, 162, 140
- King I., 1962, *AJ*, 67, 471
- Koenig X.P., Leisawitz D.T., 2014, *ApJ*, 791, 131
- Kroupa P., 2001, *MNRAS*, 322, 231
- Kruskal J. B. J., 1956, *Proc. Amer. Math. Soc.*, 7, 48
- Kuhn M. A., Feigelson E. D., Getman K. V., et al., 2014, *ApJ*, 787, 107
- Kuhn M.A., Feigelson E. D., 2017, in the *Handbook of Mixture Analysis*, edited by S. Frühwirth-Schnatter, G. Celeux, and C. P. Robert (Chapman & Hall/CRC), ISBN 9780367732066
- Kuhn M. A., Getman K. V., Feigelson E. D. et al., 2017, *AJ*, 154, 214
- Kuhn M. A., Hillenbrand L. A., Sills A., Feigelson E. D., Getman K. V., 2019, *ApJ*, 870, 32
- Lada C. J., Lada E. A., 2003, *ARA&A*, 41, 57
- Li L., Shao Z., Li Z.-Z. et al., 2020, *ApJ*, 901, 49
- Liu L., Pang X., 2019, *ApJS*, 245, 32
- Liu J., Fang M., Tian H. et al., 2021, *ApJS*, 254, 20
- Luri X., Brown A. G. A., Sarro L. M. et al., 2018, *A&A*, 616, A9
- Maia F. F., Dias B., Santos Jr J. F. et al., 2019, *MNRAS*, 484, 5702
- Marigo P., Girardi L., Bressan et al., 2017, *ApJ*, 835, 77
- Marsh K. A., Whitworth A. P., Lomax O., 2015, *MNRAS*, 454, 4292
- Marsh K. A., Whitworth A. P., Lomax O. et al., 2017, *MNRAS*, 471, 2730
- Maschberger T., Clarke C. J., 2011, *MNRAS*, 416, 541
- Maurya J., Joshi Y. C., Gour A. S., 2020, *MNRAS*, 495, 2496
- Minniti D., Lucas P. W., Emerson J. P. et al., 2010, *New Astron.*, 15, 433
- Molinari S., Swinyard B., Bally J. et al., 2010, *PASP*, 122, 314
- Monteiro H., Dias W. S., Moitinho A., Cantat-Gaudin T., Lépine J. R. D., Carraro G., Paunzen E., 2020, *MNRAS*, 499, 1874
- Navarete F., Galli Ph.A.B., Daminieli A., 2019, *MNRAS*, 487, 2771
- Navarete F., Daminieli A., Ramirez A. E., Rocha D. F., Almeida L. A., 2022, *MNRAS*, 516, 1289
- Nony T., Robitaille J. F., Motte F. et al., 2021, *A&A*, 645, A94
- O'Donnell J. E., 1994, *ApJ*, 422, 158
- Ochsenbei, F.; Bauer P.; Marcout J., 2000, *A&AS*, 143, 23
- Pang, X., Tang S-Y., Li Y. et al., 2022, *ApJ* 931, 156
- Parker R. J., 2018, *MNRAS*, 476, 617
- Parker R. J., Wright N. J., Goodwin S. P., Meyer M. R., 2014, *MNRAS*, 438, 620
- Parker R. J., Goodwin S. P., 2015, *MNRAS*, 449, 3381
- Parker R. J., Alves de Oliveira C., 2023, *MNRAS*, 525, 1677
- Parker R. J., Schoettler C., 2022, *MNRAS*, 510, 1136
- Piatti A. E., 2014, *MNRAS*, 445, 2302
- Poggio E., Drimmel R., Cantat-Gaudin T. et al., 2021, *A&A*, 651, A104
- Pouteau Y., Motte F., Nony T. et al., 2023, *A&A*, 674, A76
- Press W. H., Teukolsky S. A., Vetterling W. T., Flannery B. P., 2007, *Numerical recipes: the art of scientific computing*, 3 edn. Cambridge University Press, Cambridge, UK
- Rain M. J., Ahumada J. A., Carraro G., 2021, *A&A*, 650, A67
- Ray A., Frinchaboy P., Donor J. et al., 2022, *AJ*, 163, 195
- Richer H. B., Caiazzo I., Du H. et al., 2021, *ApJ*, 912, 165
- Rodríguez M. J., Feinstein C., Baume G. et al., 2023, *MNRAS*, 519, 3357
- Rubinstein R. Y., 1997, *Eur. J. Operat. Res.*, 99, 89
- Saito R. K., Hempel M., Minniti, D. et al., 2012, *A&A*, 537, A107
- Sanders W. L., 1971, *A&A*, 14, 226
- Santos J. F. C. J. et al., 2020, *MNRAS*, 498, 205
- Santos-Silva T., Gregorio-Hetem J., 2012, *A&A*, 547, A107
- Santos-Silva T., Perottoni H. D., Almeida-Fernandes F. et al., 2021, *MNRAS*, 508, 1033
- Savage B. D., Mathis J. S., 1979, *ARA&A*, 17, 73
- Schmeja S.; Klessen R. S., 2006, *A&A*, 449, 151
- Schmeja S., Gouliermis D.A., Klessen R. S., 2009, *ApJ*, 694, 367
- Schoettler C., Parker R. J., de Bruijne J., 2022, *MNRAS*, 510, 3178
- Skrutskie M.F., Cutri R.M., Stiening R. et al., 2006, *AJ*, 131, 1163
- Song F., Esamdin A., Hu Q., Zhang M. 2022, *A&A*, 666, A75
- Spina L., Ting Y. -S., De Silva G. M. et al., 2021, *MNRAS*, 503, 3279
- Tarricq Y., Soubiran C., Casamiquela L. et al., 2022, *A&A*, 659, A59
- Uribe A., Brieva E., 1994, *Ap&SS*, 214, 171
- Vicente B., Sánchez N., Alfaro E. J., 2016, *MNRAS*, 461, 2519
- Wenger M., Ochsenbein F., Egret D. et al., 2000, *A&AS*, 143, 9
- Wright E.L., Eisenhardt P.R.M., Mainzer A.K. et al., 2010, *AJ*, 140, 1868
- Yen S.X., Reffert S., Schilbach E., Röser S., Karchenko N.V., Piskunov A.E., 2018, *A&A*, 615, A12

APPENDIX A: CIRCUMSTELLAR EMISSION

The identification of cluster members showing infrared (IR) emission is based on the *WISE* colours diagram using photometry at $3.4\ \mu\text{m}$, $4.6\ \mu\text{m}$, and $12\ \mu\text{m}$ that is commonly adopted to distinguish between disc-bearing stars and pre-main sequence (PMS) stars without discs. Koenig & Leisawitz (2014) proposed limits on the $[3.4\ \mu\text{m} - 4.6\ \mu\text{m}] \times [4.6\ \mu\text{m} - 12\ \mu\text{m}]$ diagram defining the expected locus for Class I and Class II objects, which are PMS with the presence of protoplanetary disc, as indicated by their significant IR-excess. On the other hand, field stars and Class III PMS objects lacking dust discs do not show IR emission and are well separated in the *WISE* colours diagram.

Following the methodology described by Gregorio-Hetem et al. (2021), we extracted from the *AllWISE* catalogue only the sources with good photometry quality at band *W3* ($12\ \mu\text{m}$) and avoiding contamination from fake detections, according with the filters proposed by Koenig & Leisawitz (2014): $0.45 < W3_{r\chi^2} < 1.15$ and $W3_{snr} > 5$, where $r\chi^2$ and snr correspond to the photometric error and signal-to-noise ratio, respectively.

In Fig. A1 (top panel), we show the *WISE* colours diagram for all the cluster members that were selected from the *AllWISE* catalogue. As expected for the older clusters, most objects do not exhibit an IR-excess and are located within the region of Class III or field stars, indicating the lack of protoplanetary disc.

Only 13 objects belonging to the youngest clusters of our sample appear in the region of disc-bearing stars (Class I and Class II). Nine of them are members of Col205, which corresponds to a significant fraction of disc-bearing stars (11 percent), considering the number of members we studied. For young clusters at this age (42 Myr), it is observed a lower fraction of disc-bearing stars (e.g. Hernández et al. 2008; Fedele et al. 2010). In the case of NGC2659a (30 Myr old), we found only 3 Class II objects, meaning a fraction of 3 percent of stars with disc, more compatible with other clusters of the same age. The other Class II object is member of NGC 2168, whose low fraction (0.1 percent) of disc-bearing stars is in agreement with the age 119 Myr found for this cluster

The bottom panel of Fig. A1 displays a similar diagram showing the $[H-K]$ colour from *2MASS* as a function of $[3.4\ \mu\text{m} - 4.6\ \mu\text{m}]$, which confirms the low-level of IR emission for most members of the studied clusters. Once the diagrams in Fig. A1 are constructed for cluster members, we suggest that the lacking-disc stars of our sample are Class III objects. That means, once they have a high membership probability, they can be distinguished from MS field stars.

APPENDIX B: ADDITIONAL FIGURES

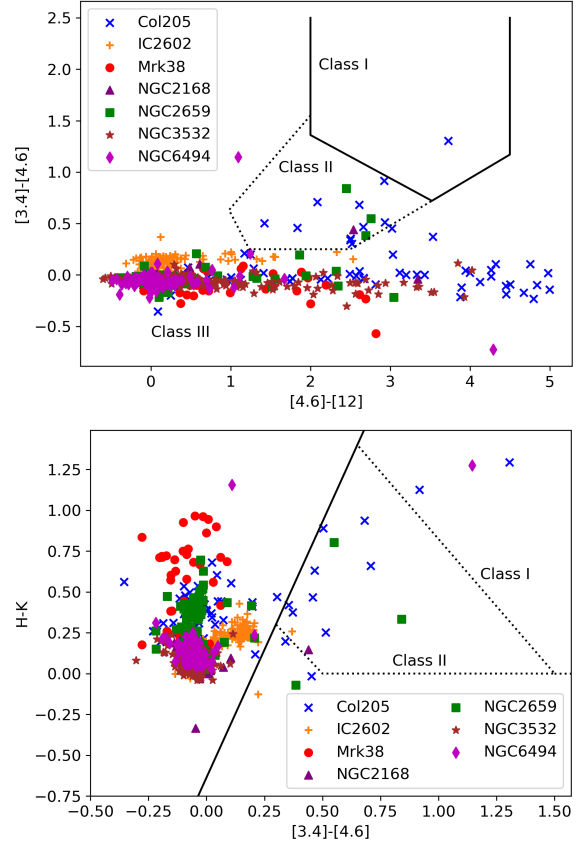


Figure A1. *Top:* *WISE* colour-colour diagram displaying the expected locus for disc-bearing stars (Class I and Class II sources). Most of the members of our clusters are found in the region of Class III objects, with no dust emission from protoplanetary discs. *Bottom:* The separation of objects from Classes I, II and III shown by *2MASS* and *WISE* colours.

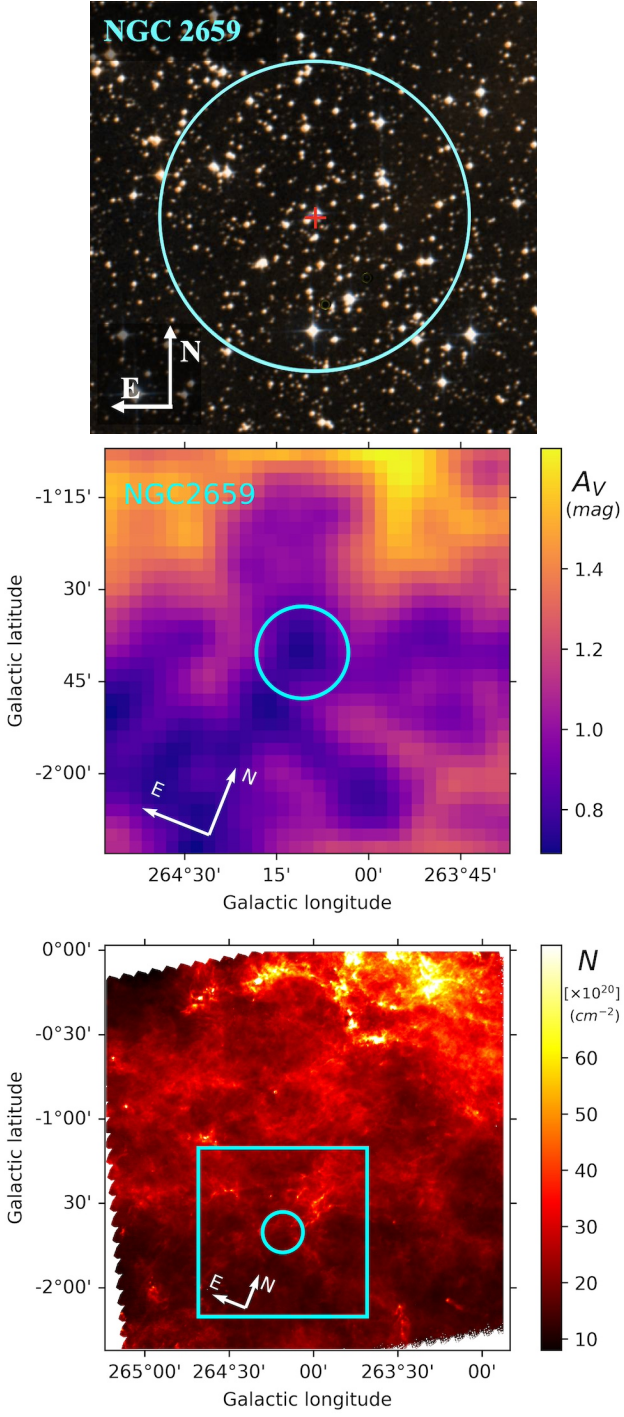


Figure B1. The same as Fig. 1 for NGC 2659. *Top:* DSS optical image. *Middle:* Visual extinction map. (*Bottom:* Integrated column density map of hydrogen molecules estimated from (*Herschel*-PPMAP). The cyan square approximately corresponds to the same area seen in the middle panel.

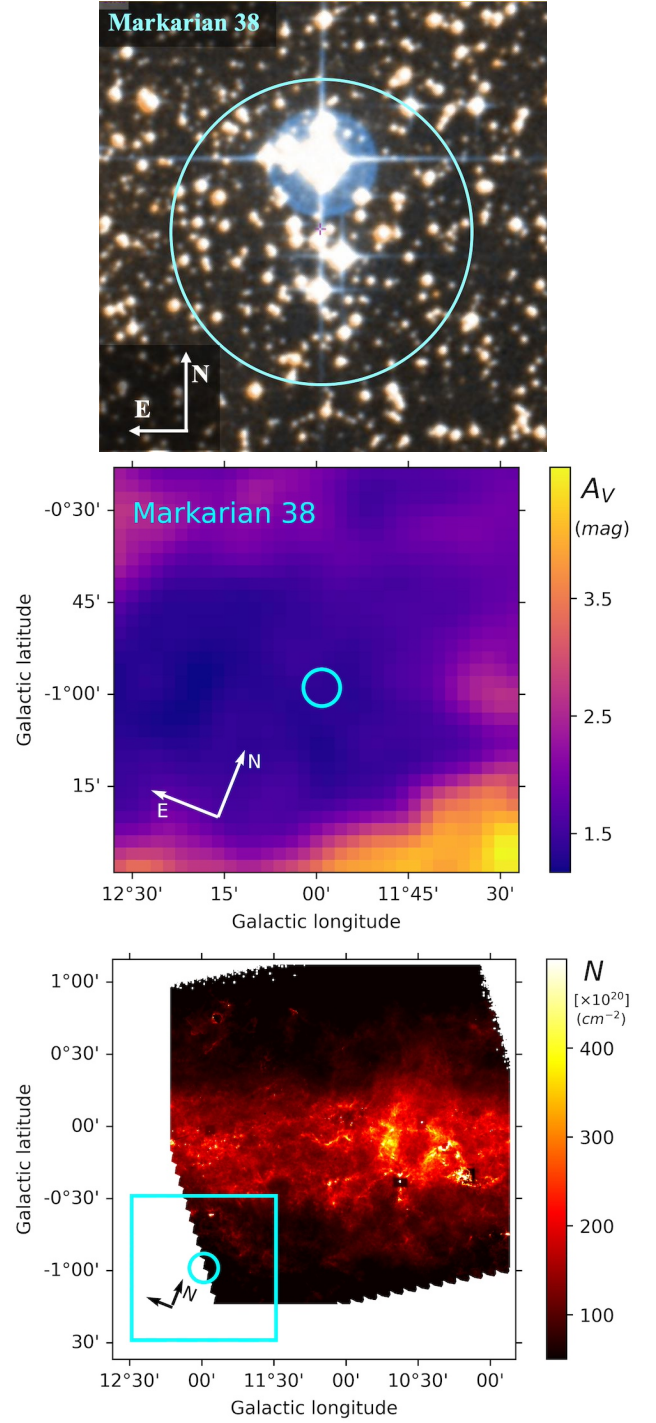


Figure B2. The same as Fig. B1 for Mrk38.

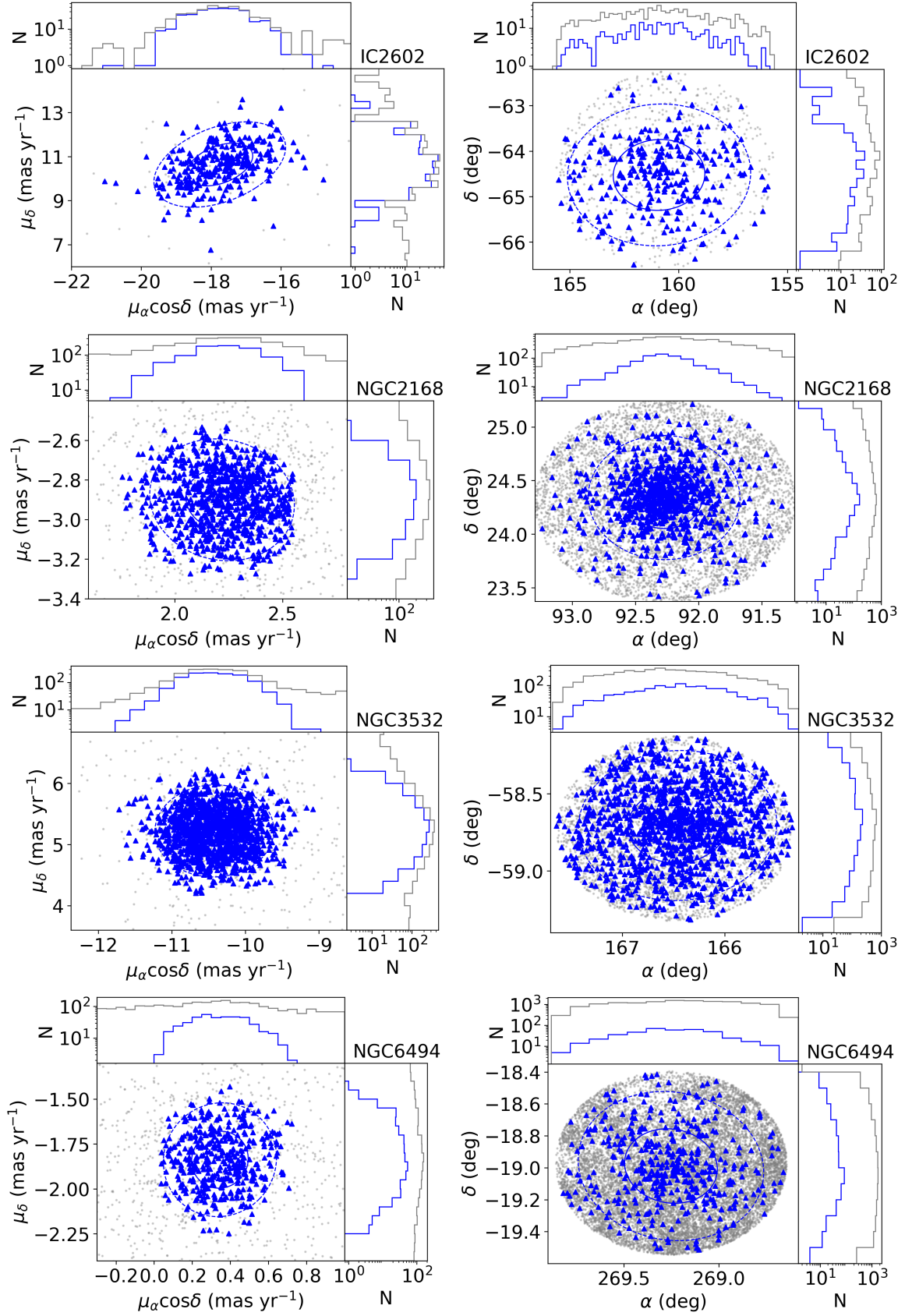


Figure B3. The same as Fig. 2.

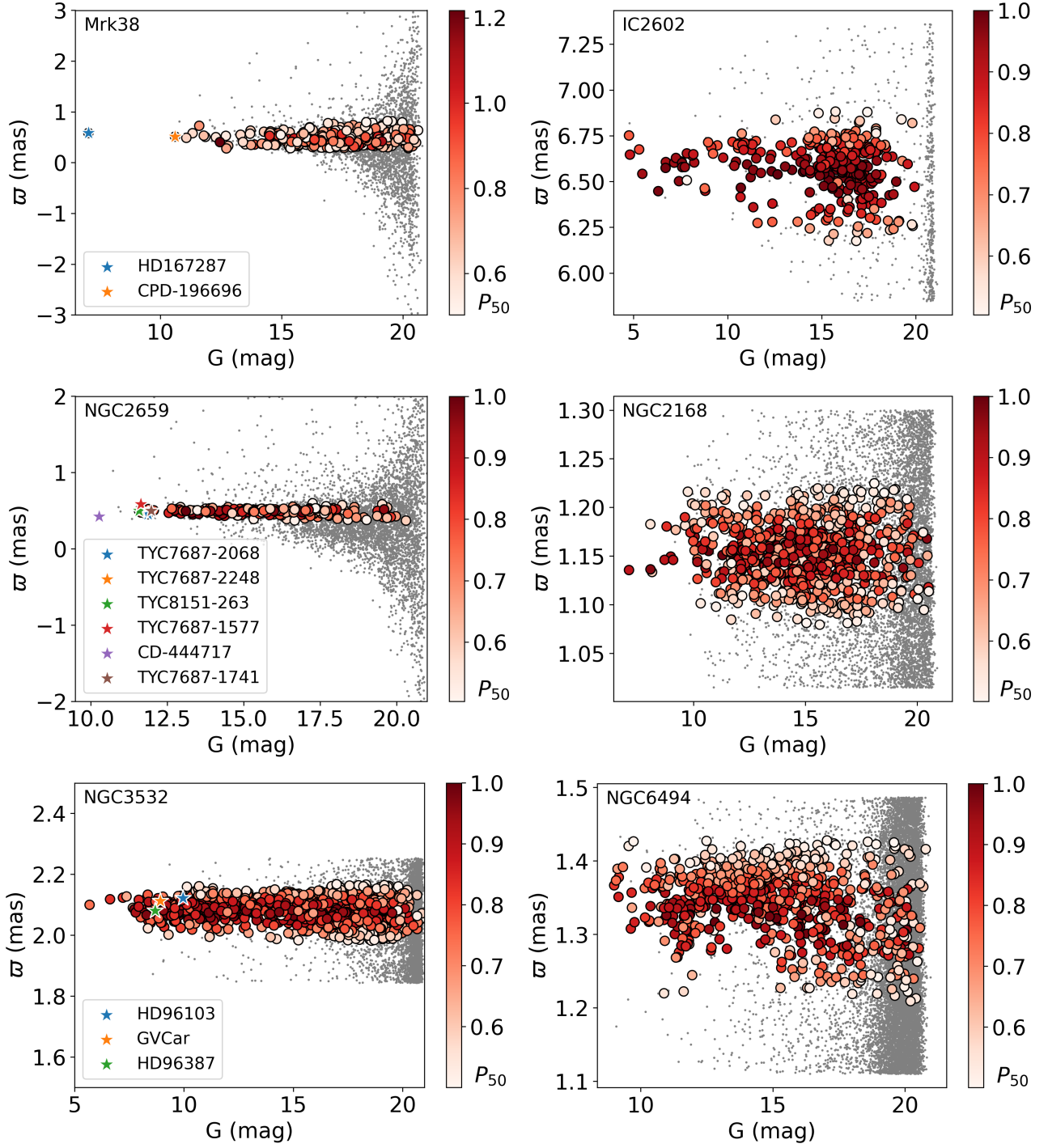


Figure B4. The same as Fig. 3.

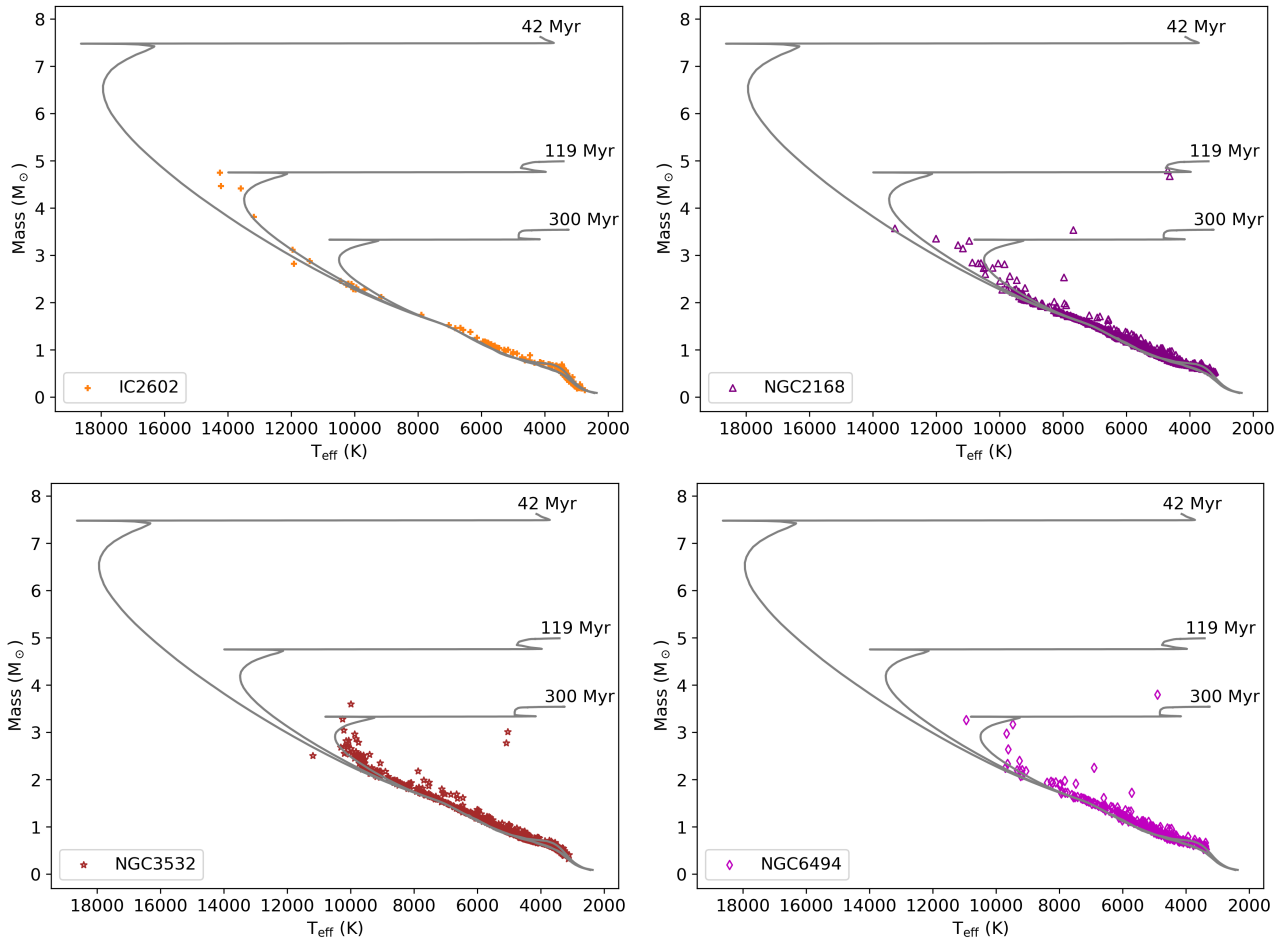


Figure B5. The same as Fig. 6.

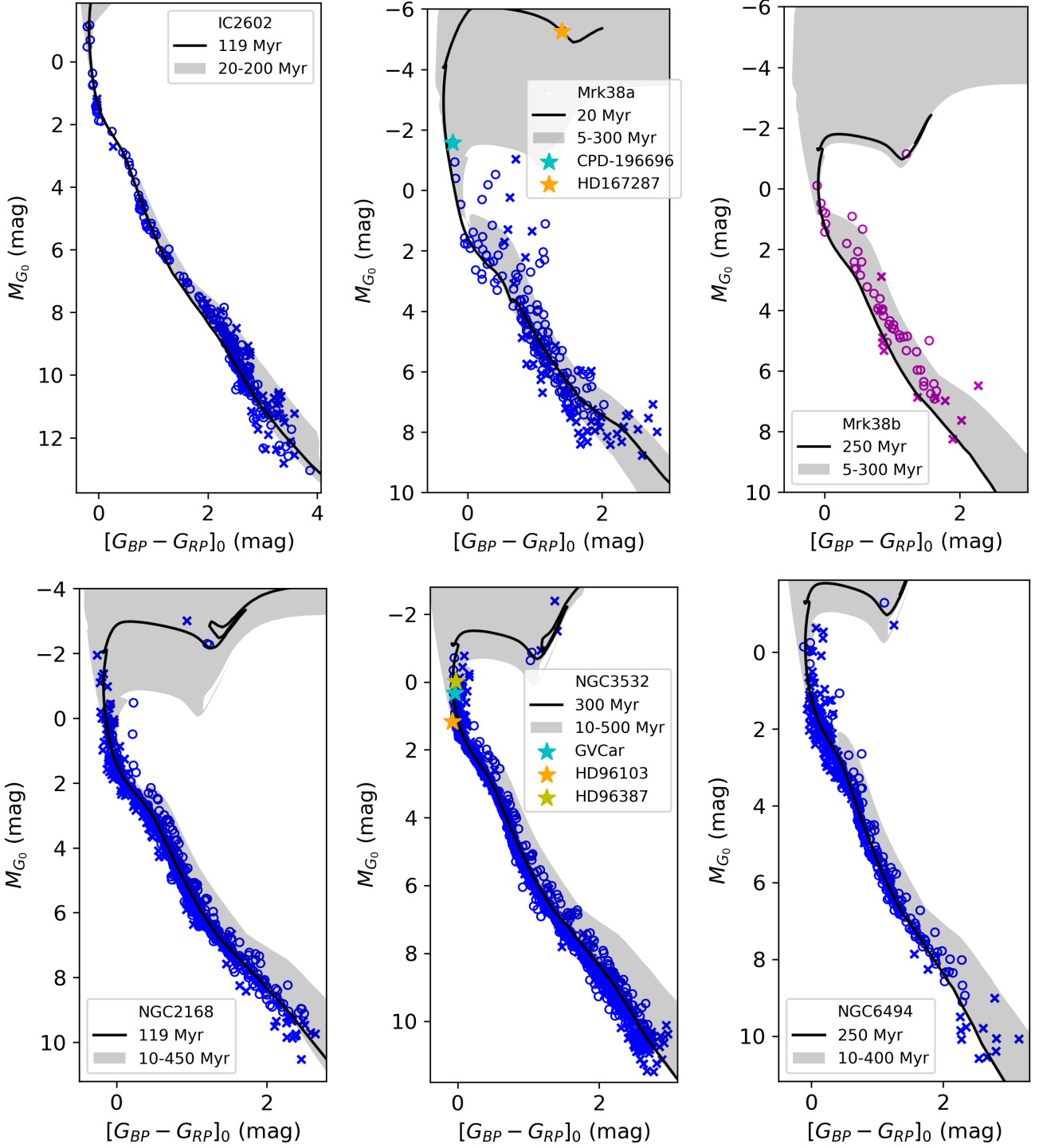


Figure B6. The same as Fig. 5.

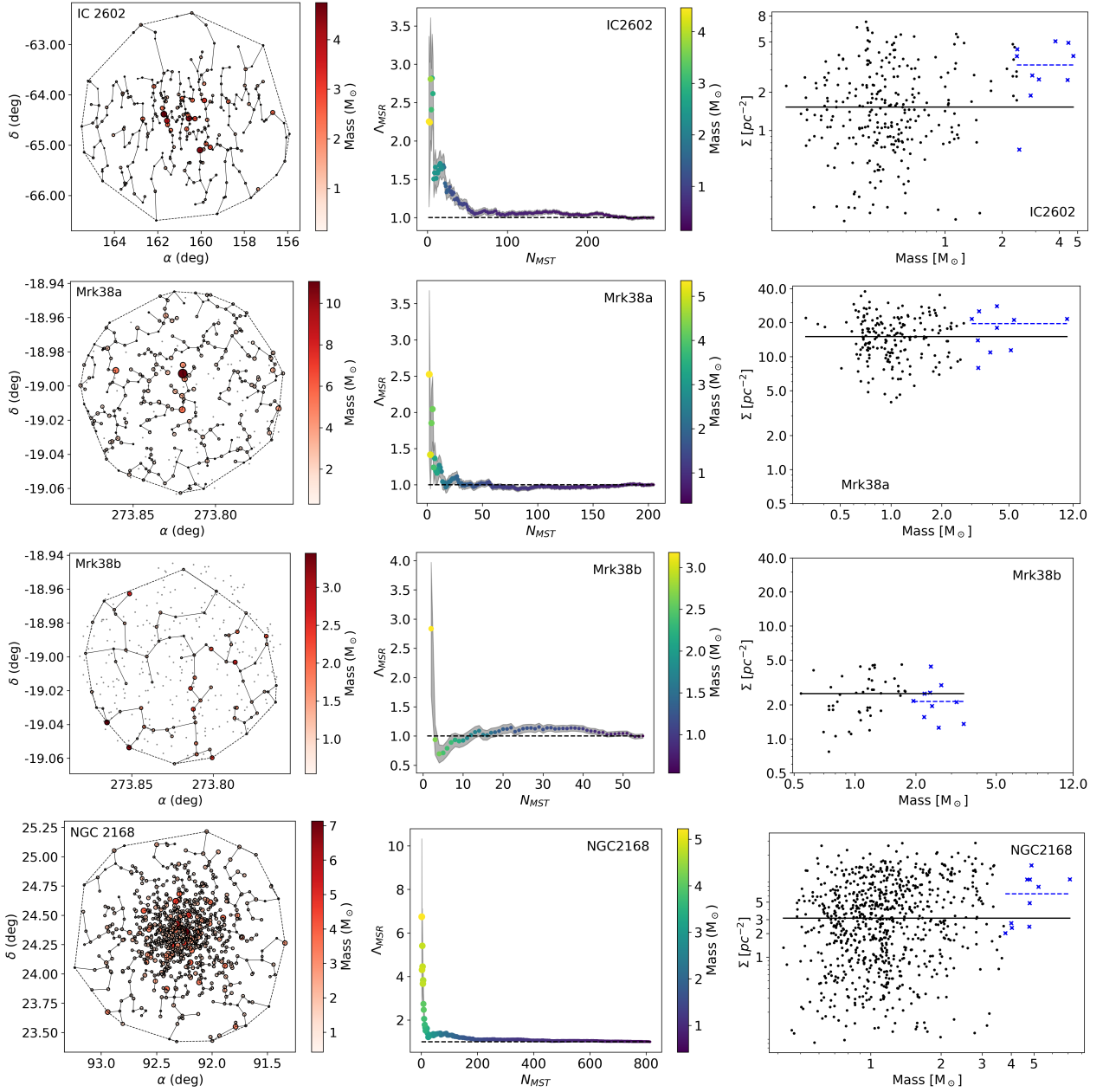


Figure B7. The same as Fig. 8. For comparison, only the $\Sigma - m$ plots for Mrk38a and Mrk38b are displayed at the same scale. To evidence the offset between the full line (average obtained for all the cluster members) and the dashed line (average estimated for the 10 most massive stars), the same scale is not adopted for all the other clusters since a clear separation between these lines would not appear in the plots.

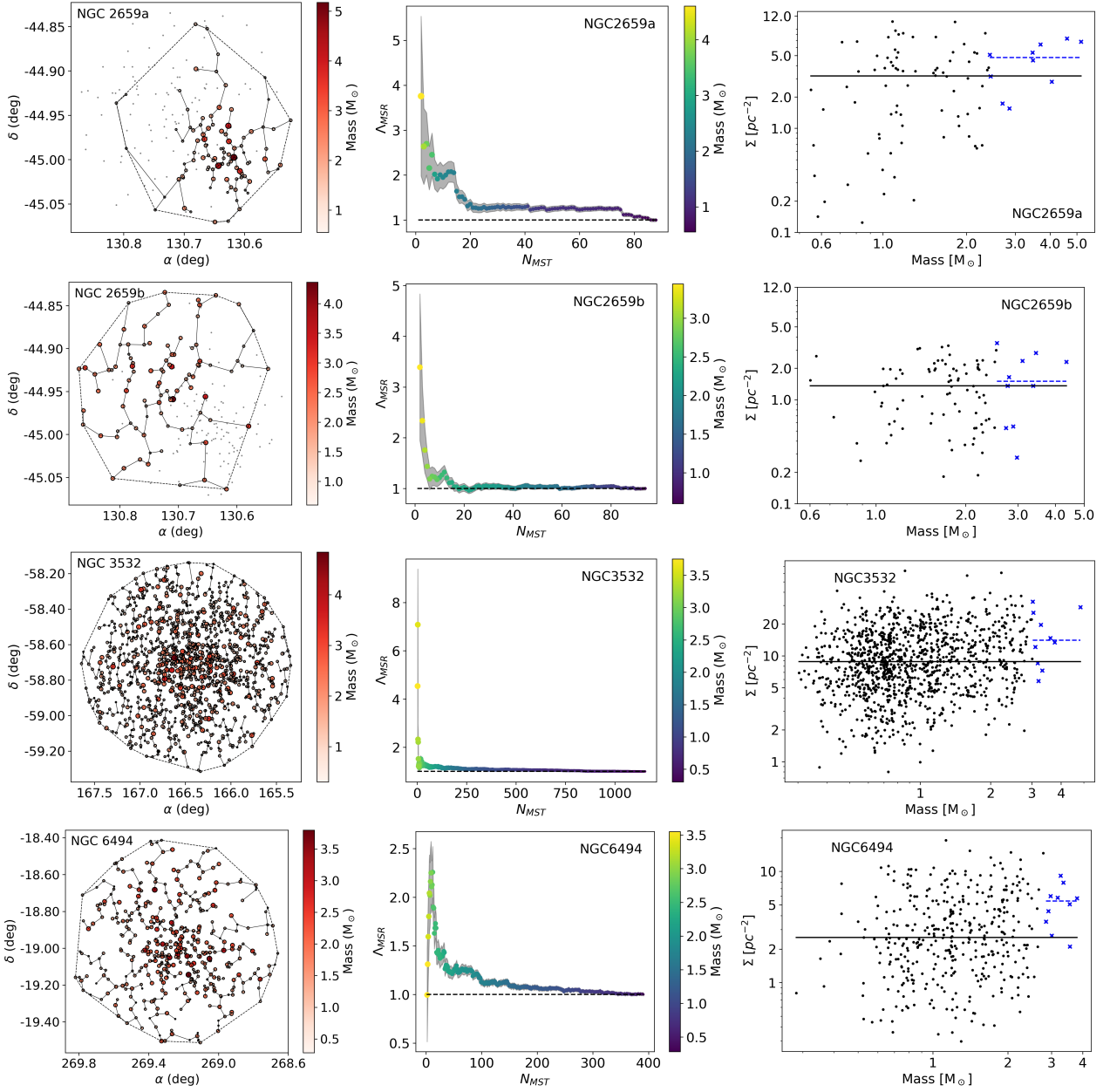


Figure B8. Continuation of Fig. B7. For comparison, only the $\Sigma - m$ plots for NGC 2659a and NGC 2659b are displayed at the same scale